ORNL/TM-8752
Dist. Category UC-20 g

ORNL/TM--8752

DE83 016346

Fusion Energy Division

EQUILIBRIUM AND STABILITY PROPERTIES OF HIGH-BETA TORSATRONS

B. A. Carreras,[a] H. R. Hicks,[b] J. A. Holmes,[b]
V. E. Lynch,[b] L. Garcia,[a] J. H. Harris,[a]
T. C. Hender,[a] and B. F. Masden[b]

[a]Fusion Energy Division.

[b]UCC-ND Computer Sciences.

Date Published - August 1983

Prepared by the
OAK RIDGE NATIONAL LABORATORY
Oak Ridge, Tennessee 37830
operated by
UNION CARBIDE CORPORATION
for the
DEPARTMENT OF ENERGY
under Contract No. W-7405-eng-26

CONTENTS

ABSTRACT

Equilibrium and stability properties of high-beta torsatrons have been investigated using numerical and semianalytical techniques based on the method of toroidal averaging. The averaged equilibria have been compared with those obtained using full three-dimensional codes. Good agreement is obtained, thus validating the averaged method approach. We have studied the stability of plasmas for configurations with different aspect ratios and numbers of field periods. The role of the vertical field has also been studied in detail. The main conclusion is that for moderate aspect ratio torsatrons ($A_p \lesssim 8$), the self-stabilizing effect of the magnetic axis shift is large enough to open a direct path to the second stability region.

I. INTRODUCTION

The torsatron has been found to be an attractive experimental realization of the stellarator concept.[1-3] Since it requires only ℓ helical conductors carrying unidirectional currents to produce a field having poloidal multipolarity ℓ and does not require external toroidal field coils, it is simpler to construct, heat, and diagnose than an equivalent classical stellarator having 2ℓ helical windings and toroidal field coils. The torsatron is particularly attractive for the production of moderate-to-high shear fields, since it is feasible to pack many field periods on a torus while retaining good access.

The calculation of the magnetohydrodynamic equilibrium and stability properties is complicated (as it is for all stellarators) by the three-dimensional nature of the magnetic field. A way to circumvent the full three-dimensional problem is the method of averaging.[4] This method relies on the separation between a nearly uniform toroidal magnetic field component B_T and a toroidally fluctuating component $\vec{B}_v$ due to the external field. The method can be applied if $|\vec{B}_v|/B_T \equiv \delta << 1$ and the toroidal scale length of the fluctuation is small. This method was first applied to the stellarator equilibrium problem by Green and Johnson.[5] Their formalism, the stellarator expansion, relies on an expansion of the equilibrium equations in the inverse aspect ratio ε, taking $\varepsilon \sim \delta^2$. The stability of the equilibria with respect to modes whose extent along field lines is long compared with a field period can then be studied using a reduced set of averaged magnetohydrodynamic equations[6-8] or an energy principle.[9]

More recently, two new approaches to simplify the three-dimensional problem have been developed. Kovrizhnykh and Shchepetov[10] do the direct averaging of the magnetohydrodynamic equations without inverse aspect ratio expansion. Alternatively, Mikhailov[11] assumes that the dominant effect of finite beta is the magnetic axis shift plus a deformation of the flux surfaces once the equilibrium has been expressed in the line coordinate system in which vacuum magnetic field lines are straight. This last approach, although broader in scope than the averaging method,[12] so far has led to equivalent results.[13] These two approaches give the stellarator expansion results in the large aspect ratio limit. In the present study, the averaging techniques are applied to a variety of actual torsatron configurations (rather than model fields) in order to compute equilibria that can be readily validated by comparison to numerically computed three-dimensional equilibria.

One important property of torsatron configurations is the self-stabilizing effect[10] due to the large magnetic axis shift that occurs with increasing beta. For some of these configurations, this leads to the existence of a second stability regime.[7,14] In this paper, we present stability results for systematic scans of magnetic configurations. The stability is examined using the reduced set of magnetohydrodynamic equations. The results of these computations show that for systems with sufficiently low aspect ratio and moderate shear, the magnetic well produced by the outward equilibrium shift is sufficient to allow direct access to the second stability regime. The parameters of the (Advanced Toroidal Facility) ATF-1[15] device to be

constructed at Oak Ridge National Laboratory were chosen to have these properties.

A brief description of the vacuum configurations is given in Sec. II. The equilibrium calculations are presented in Sec. III, and they are compared with results from the three-dimensional computations. The stability calculations for a sequence of configurations with constant helical pitch are described in Sec. IV, and in Sec. V the effect of the external vertical field on the stability is discussed. Finally, the conclusions are presented in Sec. VI.

II. VACUUM MAGNETIC FIELD CONFIGURATIONS

A set of realistic coil configurations provides the starting point for the calculations presented here. In the case of an $\ell = 2$ torsatron, the configuration consists of two helical conductors, carrying current in the same direction and wound on a torus of major radius R_c, with a winding law

$$\zeta = \frac{\ell}{M} (\theta - \alpha \sin\theta) \ .$$

Here ζ and θ are the toroidal and poloidal angles, respectively. In this paper we consider only circular cross-section coils having radius a_c. The modulation parameter α can be varied to modify the vacuum well depth, although in this paper $\alpha = 0$ is used. An additional external vertical magnetic field must be provided to define the location of the magnetic axis and allow closed magnetic surfaces to form. The main coil parameters used in the equilibrium and stability studies are the coil aspect ratio $A_c = R_c/a_c$, the number of field periods M, and the

coil pitch parameter $p_c = M/(\ell A_c)$. By changing these parameters, the main physics characteristics of the vacuum configuration, namely the rotational transform γ, the shear, the well depth, and the shape of the vacuum flux surfaces, can be varied.

For the numerical calculations, each helical conductor is represented by a filamentary winding consisting of approximately 200 straight elements. In a few cases, up to 8 filaments have been used to simulate the finite cross section of each coil. Details on the numerical implementation of the vacuum field calculations as well as the equilibrium and stability calculations will be given elsewhere.[16]

Many of the configurations studied in this paper lie on a constant-pitch line, $p_c = 1.4$, which is a result of the interrelationship of pitch, shear, and flux surface aspect ratio. This value of pitch gives moderate shear, large flux surface radius, and large transform over the region of closed flux surfaces, all of which make this family of configurations appealing for experimental purposes. In this paper, constant-pitch scans are used to investigate equilibrium and stability properties as a function of aspect ratio. The effect of changing the pitch is illustrated in Fig. 1. This figure shows three configurations with the same coil aspect ratio and different M. The lowest-pitch case with M = 10 has small flux surfaces and no shear. The highest-pitch case with M = 15 has large volume utilization but high transform only on the outer surfaces, which are lost when finite-size coils are used and allowance is made for plasma-wall spacing. The case with M = 12 and $p_c = 1.4$ is a good compromise between plasma size, shear, and transform. As will be shown, the stability properties also favor such a pitch line. Figure 2 shows some

of the configurations studied in the constant-pitch ($p_c = 1.4$) scan, together with their vacuum rotational transform profiles. For this scan, only configurations with $M \geq 8$ are considered. For smaller values of M, the magnetic axis of the vacuum configuration bifurcates, and therefore the techniques discussed in this paper cannot be applied.

We have also investigated the effect of variation of the external vertical magnetic field on the equilibrium and stability properties of torsatron configurations. The inclusion of vertical field coils allows the magnetic field configuration to be varied by changing the position of the magnetic axis. When the position of the vacuum magnetic axis relative to the geometrical center of the coils, Δ_v, changes from positive (outwards) to negative (inwards) (Fig. 3), the magnetic configuration changes from one with a vacuum magnetic well to one with a magnetic hill (Fig. 4).

III. EQUILIBRIUM CALCULATIONS

In this section, different ways of applying the averaged method to equilibrium calculations are discussed. Then these results are compared to the results from the Chodura-Schlüter[17] and NEAR[13] three-dimensional equilibrium codes.

Following the approach of Kovrizhnykh and Shchepetov,[10] the magnetic field $\vec{B}$ is expressed as a superposition of two components – $\langle\vec{B}\rangle$, which varies slowly with ζ, and $\tilde{\vec{B}}$, which oscillates rapidly with ζ:

$$\vec{B} = \langle\vec{B}\rangle + \tilde{\vec{B}} . \qquad (1)$$

Particularly for equilibrium calculations, $\langle \vec{B} \rangle$ is taken to be axisymmetric. The notation $\langle\rangle$ is used to indicate toroidal angle averages over a field period; that is,

$$\langle f \rangle = \frac{M}{2\pi} \int_0^{2\pi/M} f(\vec{r}) d\zeta \ . \tag{2}$$

The rapidly oscillating part of the magnetic field is defined such that $\langle \tilde{\vec{B}} \rangle = 0$. In toroidal geometry we use either the usual cylindrical coordinate system (R, Z, ζ) or the (r, θ, ζ) system, with $R = R_0 + r \cos\theta$ and $Z = r \sin\theta$, where $R_0 = R_c + \Delta_v$. For the averaged magnetic field we use the representation

$$\langle \vec{B} \rangle = \frac{1}{R} \vec{\nabla}\Psi_0 \times \hat{\zeta} + \frac{F}{R} \hat{\zeta} \ , \tag{3}$$

where $\hat{\zeta}$ is the unit vector in the toroidal direction.

The oscillating part of the magnetic field is assumed to be equal to the oscillating part of the vacuum field component $\tilde{\vec{B}}_v$, neglecting terms of order $\varepsilon\delta$. Therefore,

$$\tilde{\vec{B}} = \vec{\nabla}\chi \ , \tag{4}$$

where χ is the solution of the Laplace equation,

$$\vec{\nabla}^2\chi = 0 \ , \tag{5}$$

in a domain that does not enclose any coils. The boundary condition is $\hat{n} \cdot \vec{\nabla}\chi = \hat{n} \cdot \tilde{\vec{B}}_v$, where $\hat{n}$ is the unit vector perpendicular to the

boundary of the domain in which Eq. (5) is solved. The solution of Eq. (5) satisfies $\langle \chi \rangle = 0$. In general, the vacuum field has a nonoscillatory component apart from the dominant toroidal field. This can be caused, for example, by a vertical or multipolar field. Thus, the total vacuum field is expressed in the following fashion:

$$\vec{B}_v = \frac{1}{R} \vec{\nabla}\Psi_v \times \hat{\zeta} + \frac{F_v}{R}\hat{\zeta} + \vec{\nabla}\chi \ . \tag{6}$$

From the coil configuration described in the previous section, $\vec{B}_v$ is calculated using the Biot-Savart law. Once $\vec{B}_v$ is known, it is possible to calculate Ψ_v, F_v, and χ by Fourier-analyzing $\vec{B}_v$ and solving Eq. (5) with appropriate boundary conditions. The details of this calculation are given in Ref. 16.

Representing the vacuum field in terms of the functions χ, Ψ_v and F_v, we can proceed to solve the equilibrium equations:

$$\begin{aligned} \vec{J} \times \vec{B} &= \vec{\nabla}p \ , \\ \vec{J} &= \vec{\nabla} \times \vec{B} \ , \\ \vec{\nabla} \cdot \vec{B} &= 0 \ . \end{aligned} \tag{7}$$

Separating the nonoscillatory part of the functions from the oscillatory part and using the method of averaging as in Ref. 10, one obtains

$$\vec{\nabla}\langle p \rangle = \langle \vec{J} \rangle \times \vec{B}_{eff} - \vec{\nabla}\lambda \ , \tag{8}$$

where

$$\vec{B}_{eff} = \langle \vec{B} \rangle + \vec{B}^* ,$$

with

$$\vec{B}^* = \frac{1}{R} \vec{\nabla}\Psi^* \times \hat{\zeta} + \frac{F^*}{R}\hat{\zeta} , \tag{9}$$

$$\psi^* = - \frac{R^3}{F} \left\langle \frac{\partial^2 \bar{\chi}}{\partial R \partial \zeta} \frac{\partial^3 \bar{\chi}}{\partial Z \partial \zeta^2} \right\rangle , \tag{10}$$

$$F^* = - \frac{R^2}{F} \langle (\vec{\nabla}\chi)^2 \rangle , \tag{11}$$

$$\lambda = - \frac{F}{R^2} \frac{\langle \vec{J} \rangle \cdot \langle \vec{B} \rangle}{\langle \vec{B} \rangle^2} \Psi^* , \tag{12}$$

and $\bar{\chi}$ satisfies

$$\frac{\partial^2 \bar{\chi}}{\partial \zeta^2} = -\chi . \tag{13}$$

The derivation of Eq. (8) is given in detail in Ref. 10 and will not be repeated here. Note that

$$\vec{B}_{eff} \cdot \vec{\nabla}(\Psi_0 + \Psi^*) = 0 . \tag{14}$$

This means that the function $\Psi = \Psi_0 + \Psi^*$, the averaged value of the flux, is a flux function for the effective magnetic field. In particular, $\Psi_v^* = \Psi_v + \Psi^*$ = constant gives the averaged vacuum magnetic flux surfaces. In Fig. 5 the vacuum magnetic flux surfaces at two different toroidal angles within a field period [Fig. 5(a)] are compared with the averaged vacuum flux surfaces for the same configuration [Fig. 5(b)].

By introducing terms of order ε^2, Kovrizhnykh and Shchepetov rewrite Eq. (8) in the following way:

$$\vec{\nabla}\langle p\rangle = \langle\vec{J}\rangle \times \vec{B}_{eff} + \vec{B}_{eff} \times \left(\vec{B}_{eff} \times \frac{\vec{\nabla}\lambda}{B_T^2}\right) . \tag{15}$$

Here $B_T = F_v/R_0$. Proceeding in a somewhat different way by introducing an effective pressure term $p_{eff} = \langle p\rangle + \lambda$, Eq. (8) can be rewritten as

$$\vec{\nabla}p_{eff} = \langle\vec{J}\rangle \times \vec{B}_{eff} . \tag{16}$$

Equations (8), (15), and (16) involve only toroidally averaged quantities. These equations are equivalent to an axisymmetric equilibrium equation and can be cast in a Grad-Shafranov form. In this way the full three-dimensional problem is greatly simplified. Using Eqs. (3), (9), and (16), we finally obtain

$$\Delta^* \Psi = -R^2 \frac{dp_{eff}}{d\Psi} - \left(F + F^*\right)\frac{dF}{d\Psi} + \Delta^* \Psi_v^* . \tag{17}$$

This equation is solved numerically using the RSTEQ[18] equilibrium code, giving as input the vacuum magnetic field data, F^* and Ψ_v^*, and a $p_{eff}(\Psi)$ profile. The averaged equilibrium flux Ψ is then calculated either by requiring zero toroidal current on each Ψ surface or by specifying a rotational transform profile.

From Eq. (17) the results of the stellarator expansion[5] can be recovered by expanding the different functions and the Δ^* operator in powers of ε. To do so, it is necessary to impose the ordering $B_\perp/B_T \sim \beta \sim \varepsilon$, which implies $\Psi = \varepsilon\Psi_1 + O(\varepsilon^2)$, $p_{eff} = \varepsilon\langle p\rangle + O(\varepsilon^2)$, and $F = F_v + \varepsilon F_1 + O(\varepsilon^2)$. The equations of order ε^0 and ε are then

$$R_0^2 \frac{d\langle p\rangle}{d\Psi_1} + F_v \frac{dF_1}{d\Psi_1} = 0 \tag{18}$$

and

$$\vec{\nabla}_\perp^2 \Psi_1 = -2R_0 \times \frac{d\langle p\rangle}{d\Psi_1} - (F_1 + F^*) \frac{dF_1}{d\Psi_1} + \vec{\nabla}_\perp^2 \Psi_v^* , \tag{19}$$

where

$$\vec{\nabla}_\perp^2 f \equiv \frac{1}{r}\frac{\partial}{\partial r}\left(r\frac{\partial f}{\partial r}\right) + \frac{1}{r^2}\frac{\partial^2 f}{\partial \theta^2} . \tag{20}$$

Using Eq. (17), one can rewrite Eq. (18) as

$$\vec{\nabla}_\perp^2(\Psi_0 - \Psi_v^*) = -\left(2R_0 X - \frac{R_0^2}{F_v}F^*\right)\frac{d\langle p\rangle}{d\Psi_0} + G(\Psi_0) , \tag{21}$$

which is the equilibrium equation derived by Green and Johnson[5] and by Strauss.[6] The RSTEQ code can also numerically solve Eq. (21) using the same input and requirements as for Eq. (17).

For the configurations discussed in this paper, the equilibria obtained by solving either Eq. (17) or Eq. (21) are very similar. This is illustrated in Fig. 6, where the magnetic axis shift and magnetic well depth are plotted for equilibria with $\beta_0 = 4.3\%$, for the fixed-pitch configuration scan shown in Fig. 2. The difference in the values of the magnetic axis shift given by the two calculations is minimal, whereas differences in the well depth are more noticeable. Figure 6 also shows that the dependence of the magnetic axis shift on aspect ratio (A_p being a linear function of M, as shown in Fig. 2) is weaker than what might be expected from the simple linear estimate made using Eq. (A.1). The nonlinear effects are very important, since they cause a reduction of the rate of shift with increasing beta. It is not clear from the present results whether there is a complete saturation of the shift at large beta. This is illustrated in Fig. 7(a), where the magnetic axis shift is plotted versus peak beta β_m ($\beta_m = 2\langle p\rangle/B^2$, with $\langle p\rangle$ and B taken at the magnetic axis), for a given configuration ($M = 12$). The value of beta at the magnetic axis has been normalized to $\beta_c = 2\gamma(\bar{a})^2/A_p$. The importance of the nonlinear effects is clearly shown in this figure, which also shows that the flux-conserving calculation always gives a smaller shift than the zero-current calculation. However, this difference is smaller than that due to pressure profile effects, which are important in determining the value of the shift of the plasma magnetic axis [Fig. 7(b)].

It is interesting to compare the equilibria obtained by the method of averaging with equilibria calculated using three-dimensional codes for the same configuration. We have done such a comparison with two three-dimensional equilibrium codes: the Chodura-Schlüter[17] and the NEAR codes.[13] The results for the magnetic axis shift are plotted in Fig. 7(a). Both codes are approximately flux-conserving, and the results should be compared with the averaged method results computed using that constraint. The good agreement seen here is also apparent in comparing the magnetic flux surfaces (Fig. 8) and even in comparing the magnetic well depths (Fig. 9), which are quite sensitive to differences in equilibria. These results validate the averaged method approach.

In relation to the equilibrium properties of the configurations studied in this paper, it is necessary to comment on the different contributions to V''. We can separate the diamagnetic contribution V_D'' from the curvature contribution $V'' - V_D''$. The latter is the relevant term appearing in the Mercier stability criterion. At finite beta, the deepening of the well is mostly due to the curvature contribution, induced by the magnetic axis shift. By contrast, the diamagnetic term V_D'' is practically negligible (Fig. 10). The curvature contribution to V'' is well described by the analytic model given in the appendix using the plasma shift Δ_p obtained from the nonlinear calculation. In Fig. 10 we also compare $V'' - V_D''$, calculated from a numerical equilibrium, with $V'' - V_D'' = V_V'' + V_S''$ given by Eqs. (A.3) and (A.4).

The issue of an equilibrium beta limit is difficult to resolve. This limit is often taken to be the point at which the magnetic axis shift attains a value of one-half the minor radius. This is an arbitrary convention if taken as an absolute limit, although it is a reasonable figure of merit in comparing configurations. Another possibility is to use as a beta limit the value of beta at which the equilibrium calculation fails to find a solution. This limit may be indicative of the encroachment of a separatrix on the flux surfaces or the formation of large magnetic islands; however, it can also be due to problems arising from the numerical scheme used in solving the equilibrium equations. The limiting beta found by either criterion is also a function of the pressure profile considered, as can be inferred from Fig. 7(b), and of the assumed location of the last magnetic surface. Due to the high shear near the plasma edge, small changes of the minor radius produce important changes in $\iota(\bar{a})$, the value of the rotational transform at the plasma edge. The limiting beta, estimated by both criteria mentioned above, scales approximately as $\iota(\bar{a})^2/A_p$ and is therefore sensitive to the value of $\iota(\bar{a})$. The application of the above criteria to the M = 12 configuration in the constant-pitch scan (p_c = 1.4) gives, as a limiting beta value, $<\beta>$ = 7% to 10% and for the M = 24 case, $<\beta>$ = 10% to 16%, with the present numerical techniques.[16] Numerical calculations performed with NEAR[13] give higher values of the equilibrium beta limits for both configurations. We are currently investigating the possibility of separating the limitations on beta due to numerical resolution from intrinsic beta limitations.

IV. STABILITY RESULTS

To study the stability properties of the configurations described, we used a reduced set of magnetohydrodynamic equations[6] that includes the averaged effect of the external magnetic fields. The equations are

$$\frac{\partial \Psi}{\partial t} = -\vec{v}_\perp \cdot \vec{\nabla}\Psi - \frac{\partial \phi}{\partial \zeta} , \tag{22}$$

$$\frac{\partial U}{\partial t} = -\vec{v}_\perp \cdot \vec{\nabla}U + \frac{1}{R}\hat{\zeta} \cdot [\vec{\nabla}J_\zeta \times \vec{\nabla}\Psi] - \frac{1}{R^2}\frac{\partial J_\zeta}{\partial \zeta}$$

$$+ \frac{\beta_0}{2\varepsilon^2 R}\hat{\zeta} \cdot [\vec{\nabla} \times \Omega\vec{\nabla}\langle p\rangle] , \tag{23}$$

$$\frac{\partial \langle p\rangle}{\partial t} = -\vec{v}_\perp \cdot \vec{\nabla}\langle p\rangle , \tag{24}$$

with

$$\Omega = R^2 - 1 - F^* , \tag{25}$$

$$J_\zeta = \Delta^*(\Psi - \Psi_v) , \tag{26}$$

$$U = \nabla_\perp^2 \phi \tag{27}$$

and

$$\vec{v}_\perp = \dot{v}\phi \times \hat{\zeta} . \tag{28}$$

These equations are expressed in dimensionless form. The major radius R is normalized to R_c, $\beta_0 = 2\langle p(0)\rangle/B_0^2$, and $\hat{\zeta}$ is the unit vector in the toroidal direction. All lengths are normalized to the averaged plasma minor radius $\bar{a}$, the resistivity to η_0 (its value at the magnetic axis), the time to the poloidal Alfvén time $\tau_{hp} = R_c(\mu_0\rho_m)^{1/2}/B_0$ (where ρ_m is the mass density), the magnetic field to B_0 (the vacuum toroidal field at the center of the coil), the

velocity to $\bar{a}/\tau_{hp}$, and the averaged pressure $\langle p \rangle$ to its value at the magnetic axis. The averaged poloidal flux Ψ and the velocity stream function ϕ are normalized to $\bar{a}^2 B_0$ and $\bar{a}^2 B_0/\tau_{hp}$, respectively. The toroidal current density J_ζ/R is normalized to $B_0/\mu_0 R_c$, and U is the toroidal component of the vorticity. The toroidal component of the effective vacuum magnetic field F^* is normalized to F_v. We use a straight magnetic field line coordinate system (ρ, θ, ζ), where ρ is a label for the averaged flux surface, $0 \leq \rho \leq 1$, ζ is the toroidal angle, and the generalized poloidal angle θ is determined by requiring that the Jacobian be proportional to R^2.

These equations have been implemented in a modified version of the RST code[19] in two different ways. The first way corresponds to Eqs. (22) to (28) as written in this paper. This is compatible with the equilibrium Eq. (17). Alternately, we have taken only the terms from Eqs. (22) to (28) up to order ε, assuming $\beta_0 \sim \varepsilon$. This form corresponds to the exact form of the equations as derived in Ref. 6 and is compatible with the equilibrium Eq. (21). Stability calculations have been performed in these two ways using as input the numerical equilibria calculated by RSTEQ. The results, as in the case of the equilibrium calculations, are quite similar, with the first method giving somewhat more stable results [Fig. 11(a)].

We have used this system of equations to investigate low-n ($n = 1$ and $n = 2$ mainly), fixed-boundary ideal modes. The results for localized and high-n modes will be reported elsewhere.[20] The stability of equilibria obtained using either the flux-conserving condition or the condition of zero parallel current in each flux surface has been studied. For moderate aspect ratios, the zero current equilibria have

been found to be more stable than the flux-conserving ones [Fig. 11(b)]. This is probably due to the magnetic well. As we have seen in Fig. 7, the magnetic axis shift for the zero-current equilibrium is larger, which results in a larger curvature contribution. Henceforth, the discussion will be limited to the stability of flux-conserving equilibria.

Figure 12 shows the linear growth rates of the n = 1 and n = 2 modes for the configurations in the constant-pitch scan (Fig. 2) and for an infinite aspect ratio version of the M = 12 configuration (a helically symmetric cylinder with 12 field periods). The equilibrium pressure profile is assumed to scale as $p \propto (1 - \Psi)^2$. The infinite aspect ratio case is unstable at very low beta, as is expected from the stability studies of helically symmetric $\ell = 2$ stellarators,[21] and the linear growth rate is very large compared with the finite aspect ratio results. The M = 12 configuration, with $A_p = 7$, is stable to both n = 1 and n = 2 modes. These modes become unstable for higher A_c, higher M configurations, with growth rates increasing with M.

Examination of the harmonic spectrum of the unstable modes reveals that they are dominated by components of low-order rational helicity with singular surfaces in the plasma region. For instance, for configurations having the $\gamma = 1$ surface in the plasma, the n = 2 eigenfunction is dominated by the (m = 2; n = 2) component. The modes have a very weak ballooning character, and satellite components become less important as M and A are reduced toward configurations with $\gamma(\rho) < 1$ (Fig. 13). Figure 14 shows that the peaking of the harmonic spectra around the resonant (m = 2; n = 2) component is accompanied by a narrowing of the radial width of the eigenfunction. This change from

global to localized modes is a typical effect observed when we move toward marginal stability. This occurs not only in the constant-beta scan but also in the beta scans for a fixed configuration. This behavior adds extra difficulties to the determination of the marginal stability point, which is already difficult to determine because we use an initial value technique. Convergence studies have been necessary to assess the plasma stability near the marginal stability points. These numerical issues will be discussed elsewhere.[16]

These calculations reveal that, for moderate aspect ratio torsatrons, the location of the zero of V'' relative to the location of the low order rational surfaces is of crucial importance for stabilization. The impact of the presence of rational surfaces in the plasma upon the stability of low-n modes has already been pointed out in Ref. 10. For low-to-moderate aspect ratios, the existence of a deep magnetic well adds a new and important stabilizing effect. Figure 15(a) shows the relationship of the low-order rational surfaces to γ_c, the transform at the critical surface where $V'' = 0$, for the configurations in the constant-pitch scan. The shaded regions show where low-order rational surfaces lie in the region with $V'' > 0$ (essentially $V'' - V_D'' > 0$). In these regions the only stabilizing influence for localized modes is the shear. Figure 15(b) shows how the critical surfaces move outward as beta increases and the magnetic well deepens. Figure 15(a) shows that there is a set of $p_c = 1.4$ configurations, with $10 < M < 14$, that have favorable stability properties for low-n modes. The parameter of the ATF device were chosen in this range ($M = 12$). Similar results for the $M = 12$

configuration have been obtained applying the averaging method with the energy principle[22] and using three-dimensional techniques.[23]

V. EFFECT OF THE VERTICAL FIELD

In the previous section we studied the stability properties of configurations with the same pitch, $p_c = 1.4$, with the vacuum magnetic axis coincidental with the geometrical center of the coils. As has previously been pointed out,[10,11] the vertical field or, equivalently, the displacement of the vacuum magnetic axis plays a very important role in modifying the stability properties of a given configuration. Displacing the vacuum magnetic axis from the geometrical center of the coils modifies the vacuum magnetic well [see Eq. (A.3)]. In this section we study the impact of the vacuum magnetic axis displacement on the low-n mode stability of finite-beta plasmas.

We consider the M = 12 configuration from the constant-pitch scan. For this particular calculation, we take $R_c = 2.10$ m, by adding appropriate amounts of vertical field, we can consider a sequence of magnetic field configurations for which the magnetic axis varies from $\Delta_v = -15$ cm to $\Delta_v = 5$ cm in 5-cm steps (Fig. 3). The physical properties (transform, shear, and well, etc.) vary for these different configurations. The variations have been summarized in Fig. 4.

Equilibria have been calculated for this sequence of configurations at different beta values. The plasma magnetic axis shift for a given β is a function of Δ_v. Configurations with negative Δ_v (magnetic hill) have larger plasma shift than those with positive Δ_v (magnetic well). This effect can be seen in Fig. 16. A detailed study of these equilibria, calculated with the three-dimensional codes, will be given elsewhere.[24]

Linear growth rates for the low-n modes have been calculated by the method indicated in the previous section. In Fig. 17, the results for the n = 1 mode are shown. There is a strong stabilizing effect in going from Δ_v = -15 cm to Δ_v = -5 cm. Furthermore, the results for the Δ_v = -5 cm case suggest the existence of a second stability region[7,14] for $\beta_{tr} > 8\%$. When Δ_v goes to zero, these two stability regions merge. This shows that with an appropriate change in the vertical field there is a direct path to the second stability regime for this configuration. Such a self-stabilizing effect for this general type of configuration has already been shown, for localized high-n modes, by Kovrizhnykh and Shchepetov.[10]

VI. CONCLUSIONS

Torsatron configurations of moderate aspect ratio ($5 < A_p \leq 8$) with $10 \leq M \leq 14$ field periods are promising devices with which to experimentally investigate high-beta plasmas. The results from the study of stability of low-n modes show that direct access to the second stability regime exists. Therefore, the beta limitation for these configurations is due to equilibrium. The use of an external vertical field adds considerable flexibility to such devices and permits the exploration of stability boundaries which could give valuable information on the predictive power of the present theoretical tools.

The comparison of equilibrium calculations using the method of averaging with fully three-dimensional results gives strong support to this method. We hope to extend this type of comparison to the stability results in the near future.

APPENDIX

This appendix lists some of the expressions used in the semianalytic studies for comparison with the numerical results. They are derived in a simple manner using the stellarator expansion.[5] The plasma magnetic axis shift Δ_p, relative to the vacuum magnetic axis, in the linear approximation obeys the equation

$$\frac{1}{\rho}\frac{d}{d\rho}\left[\rho\frac{d\Delta_p}{d\rho}\right] + \frac{d\ \ell n\ (\rho^2\gamma^2)}{d\rho}\frac{d\Delta_p}{d\rho} + \left[\frac{1}{\rho^3\gamma}\frac{d}{d\rho}\left(\rho^3\frac{d\gamma}{d\rho}\right) - \frac{\beta_0}{2\varepsilon^2}\frac{1}{\rho\gamma^2}\frac{dp}{d\rho}\frac{V_v''}{\varepsilon^2}\frac{R_0}{F_v^2}\right]\Delta_p = \frac{\beta_0}{\varepsilon}\frac{1}{\rho\gamma^2}\frac{dp}{d\rho}, \tag{A.1}$$

where V_v'' is the second derivative of the volume relative to the toroidal flux for the vacuum. For nonzero beta and for an equilibrium with the same transform as the vacuum, V'' can be written as

$$V'' \equiv V_v'' + V_S'' + V_D'' \tag{A.2}$$

where

$$V_v'' = -\frac{R_0}{\varepsilon^2 F_v^2}\frac{1}{\rho}\left[\frac{d}{d\rho}\left(\frac{F^*}{F_v}\right) - \frac{\varepsilon}{\rho^2}\frac{d}{d\rho}\left(\rho^3\gamma\frac{d\Delta_v}{d\rho}\right)\right], \tag{A.3}$$

$$V_S'' = -\frac{R_0}{\varepsilon F_v^2}\left[\frac{1}{\rho^3\gamma}\frac{d}{d\rho}\left(\rho^3\frac{d\gamma}{d\rho}\right)\Delta_p + \frac{1}{\gamma^2}\frac{d\gamma^2}{d\rho}\frac{d\Delta_p}{d\rho}\right], \tag{A.4}$$

$$V_D'' = \frac{R_0}{\varepsilon^2 F_v^2}\beta_0\frac{1}{\rho}\frac{dp}{d\rho}\frac{2+\gamma^2}{2\gamma^2}, \tag{A.5}$$

are the contributions from the vacuum, plasma magnetic axis shift, and

diamagnetic contributions to V'', respectively. These expressions have been derived assuming a simple shifted-circle model for the averaged magnetic surfaces of the equilibrium.

ACKNOWLEDGMENTS

We gratefully acknowledge many useful discussions with the members of the ATF design team and in particular those with W. A. Cooper, R. A. Dory, J. F. Lyon, and J. A. Rome. We are also grateful to the Max Planck Institut für Plasmaphysik and in particular to Dr. R. Chodura for allowing the use of their three-dimensional code. We also acknowledge fruitful discussions with G. Anania, O. Betancourt, J. Johnson, P. Garabedian, and L. Kovrizhnykh.

REFERENCES

[1]C. Gourdon, D. Marty, E. K. Maschke, and J. P. Dumot, in Plasma Physics and Controlled Nuclear Fusion Research (International Atomic Energy Agency, Vienna, 1969), Vol. I, p. 847.

[2]K. Uo, J. Phys. Soc. Japan 16, 1380 (1961).

[3]I. S. Danil'kin, I. S. Shpigel, Trudy. Fiz. Inst., Akad. Nauk 65, 50 (1976) (in Russian).

[4]N. K. Bogolyubov and Yu. A. Mitropol'skij, Asymptotic Methods in the Theory of Non-Linear Oscillations (Nauka, Moscow, 1974).

[5]J. M. Green and J. L. Johnson, Phys. Fluids 4, 875 (1961).

[6]H. R. Strauss, Plasma Phys. 22, 733 (1980).

[7]H. R. Strauss and D. A. Monticello, Phys. Fluids 24, 1148 (1981).

[8]M. Wakatani, IEEE Trans. Plasma Sci. 9, 243 (1981).

[9]J. M. Green, J. L. Johnson, and K. E. Weimer, Plasma Phys. 8, 145 (1965).

[10]L. M. Kovrizhnykh and S. V. Shchepetov, Sov. J. Plasma Phys. 6, 533 (1980); L. M. Kovrizhnykh and S. V. Shchepetov, Preprint No. 36 (P. N. Lebedev Physics Institute, Academy of Sciences of the USSR, Moscow, 1980).

[11]M. I. Mikhailov, Sov. J. Plasma Phys. 6, 25 (1980).

[12]V. D. Pustovitov, Sov. J. Plasma Phys. 8, 265 (1983).

[13]T. C. Hender et al., "Torsatron Equilibria in Vacuum Flux Coordinates" (to be published).

[14]F. Bauer, O. Betancourt and P. Garabedian, Phys. Fluids 24, 48 (1981).

[15]J. F. Lyon et al., Stellarator Physics Evaluation Studies, Oak Ridge National Laboratory Report No. ORNL/TM-8496, 1983.

[16]V. E. Lynch et al. (to be published).

[17]R. Chodura and A. Schlüter, J. Comput. Phys. 41, 68 (1981).

[18]J. A. Holmes, Y.-K. M. Peng, and S. J. Lynch, J. Comput. Phys. 36, 36 (1980).

[19]V. E. Lynch, B. A. Carreras, H. R. Hicks, J. A. Holmes, and L. Garcia, Comp. Physics Commun. 24, 465 (1981).

[20]W. A. Cooper et al. (to be published).

[21]R. Chodura, R. Gruber, F. Hernegger, W. Kernor, W. Schneider, and F. Troyon, in Plasma Physics and Controlled Nuclear Fusion Research (International Atomic Energy Agency, Vienna, 1980), Vol. I, p. 813.

[22]G. Anania and J. L. Johnson, "Application of the Stellarator Expansion for Plasma Stability Studies in Stellarators" (to be published).

[23]O. Betancourt and P. Garabedian, in Proceedings of 4th International Stellarator Workshop, Cape May, New Jersey 1982 (to be published).

[24]L. Garcia et al., "Equilibrium Studies for the ATF-1 Device" (to be published).

FIGURE CAPTIONS

Fig. 1 Magnetic surfaces for torsatrons of different pitch with $A_c = 4.4$.

Fig. 2 Configurations studied in the constant-pitch scan and sample rotational transform profiles.

Fig. 3 Vacuum flux surfaces at $\zeta = 0^\circ$ (left) and $\zeta = 15^\circ$ (right) for the M = 12 configuration of the constant-pitch scan shown in Fig. 2 for different values of the vacuum magnetic axis shift Δ_V.

Fig. 4 Variation of the vacuum magnetic configuration properties with Δ_V for the same configurations as in Fig. 3.

Fig. 5 Comparison between the three-dimensional vacuum flux surfaces shown at $\zeta = 0^\circ$ and $\zeta = 15^\circ$ (top) and the corresponding averaged flux surfaces (bottom). The configuration is the same as in Fig. 3.

Fig. 6 Well depth and magnetic axis shift given by Eqs. (16) and (20) for the configurations of the fixed-pitch scan.

Fig. 7 Magnetic axis shift as a function of beta for the configuration shown in Fig. 3: (a) calculated with the different numerical codes described in the text for a given pressure profile $p \propto (1 - \psi)^2$ and (b) effect of the pressure profile on the magnetic axis shift.

Fig. 8 Comparison of torsatron equilibrium flux surfaces using different numerical techniques.

Fig. 9 Comparison of magnetic well calculated with the averaged method and the three-dimensional Chodura-Schlüter code.

Fig. 10 Different contributions to V'' at $\beta_m = 7.8\%$ for the configuration shown in Fig. 3.

Fig. 11 Linear growth rate of the $n = 2$ mode at fixed beta for different kinds of equilibrium calculations.

Fig. 12 Linear growth rates of the $n = 1$ (a) and $n = 2$ (b) ideal modes for the constant-pitch scan described in Fig. 2.

Fig. 13 M spectrum of the linear $n = 2$ eigenfunctions.

Fig. 14 Dominant Fourier component ($m = 2$) of the $n = 2$ eigenfunction for different configurations of the constant-pitch scan at $\beta_0 = 0.12$.

Fig. 15 (a) Location of low-order rational surface relative to critical surfaces of configurations in the constant-pitch scan; (b) dependence of critical surface location on beta.

Fig. 16 Magnetic axis shift versus β_m for the configurations of Fig. 4.

Fig. 17 $n = 1$ linear growth rate for the configurations described in Fig. 4.

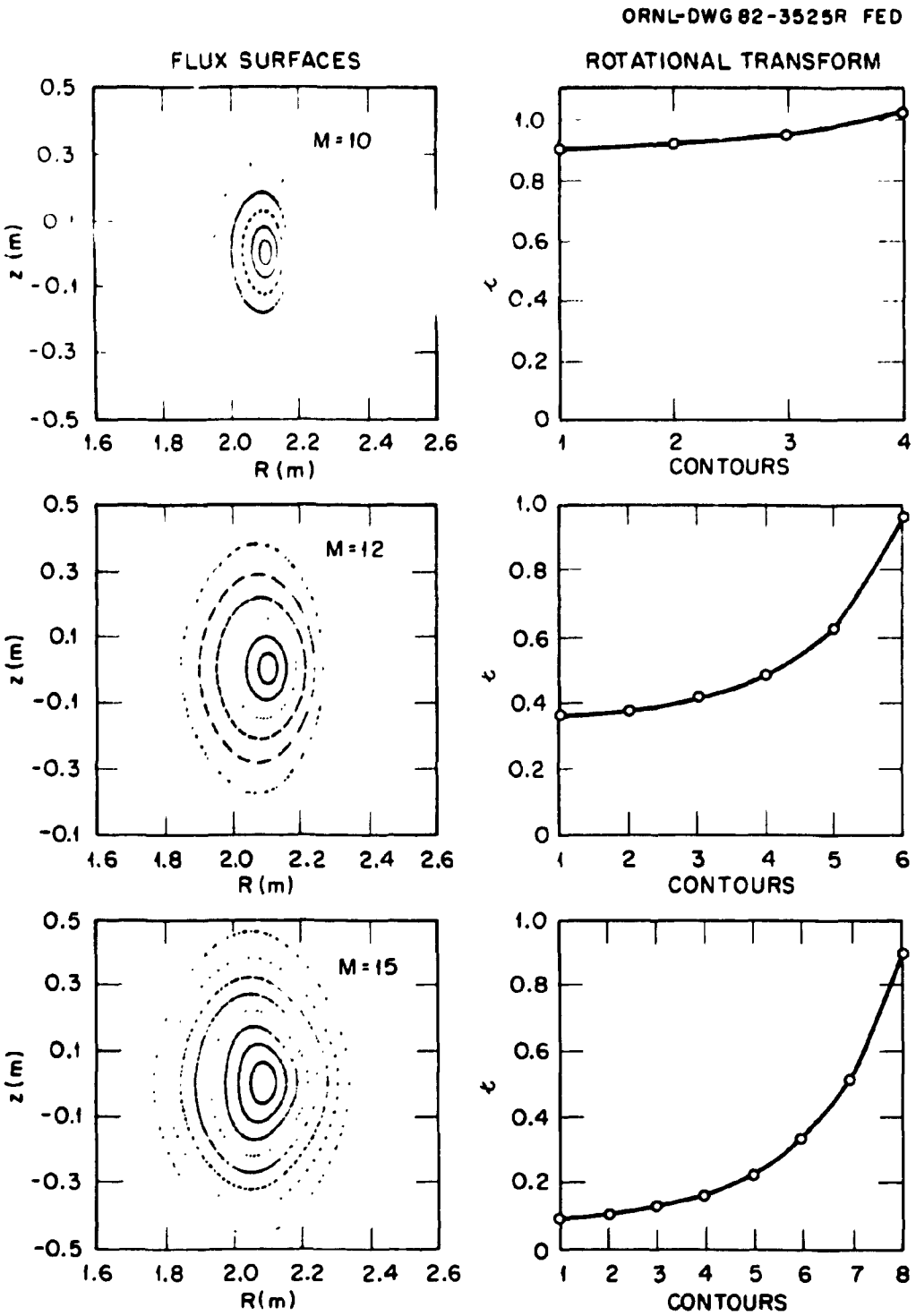
ORNL-DWG 82-3525R FED
FLUX SURFACES
ROTATIONAL TRANSFORM
M=10
M=12
M=15
z (m)
R (m)
ι
CONTOURS

Fig. 1

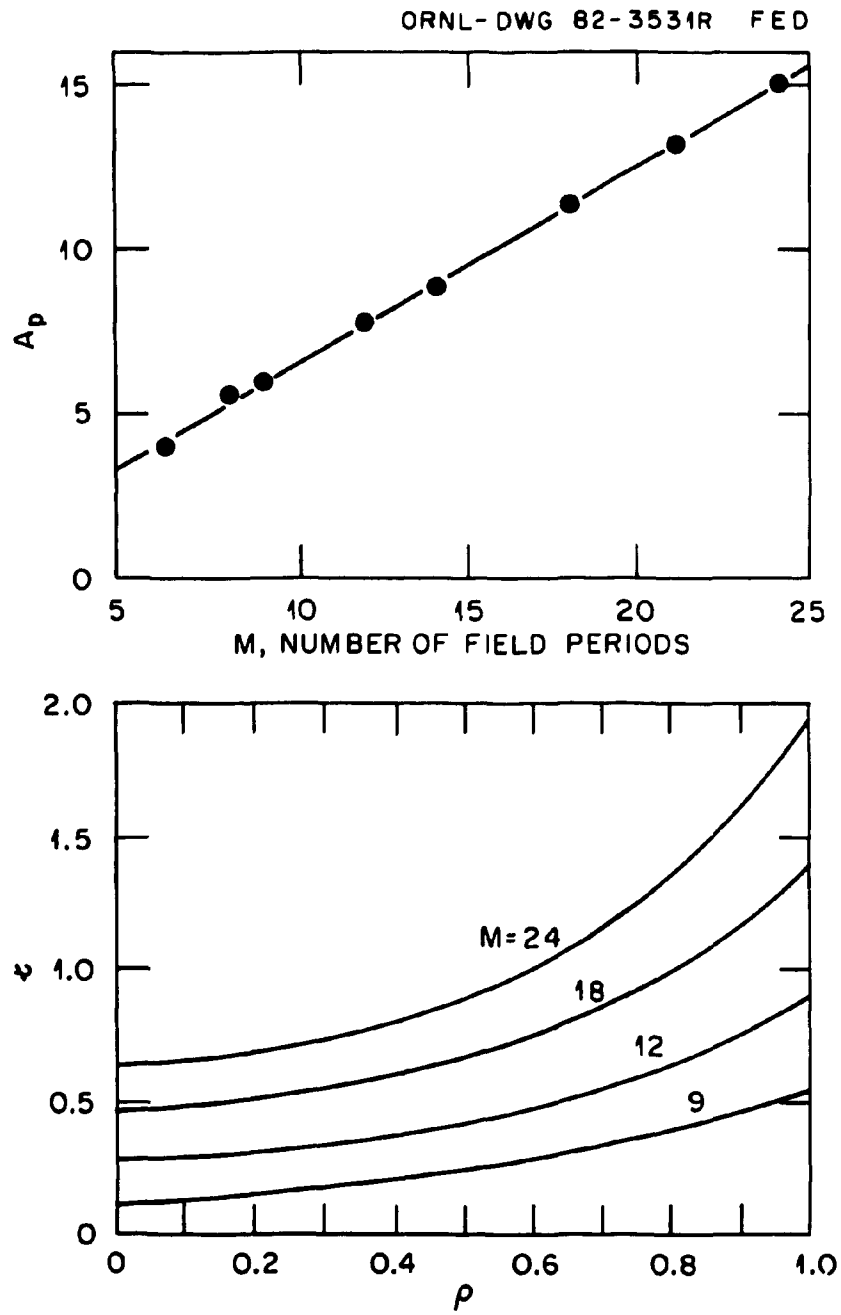
ORNL-DWG 82-3531R FED
15
10
5
0
A_p
5
10
15
20
25
M, NUMBER OF FIELD PERIODS
2.0
1.5
1.0
0.5
0
ϵ
M=24
18
12
9
0
0.2
0.4
0.6
0.8
1.0
ρ

Fig. 2

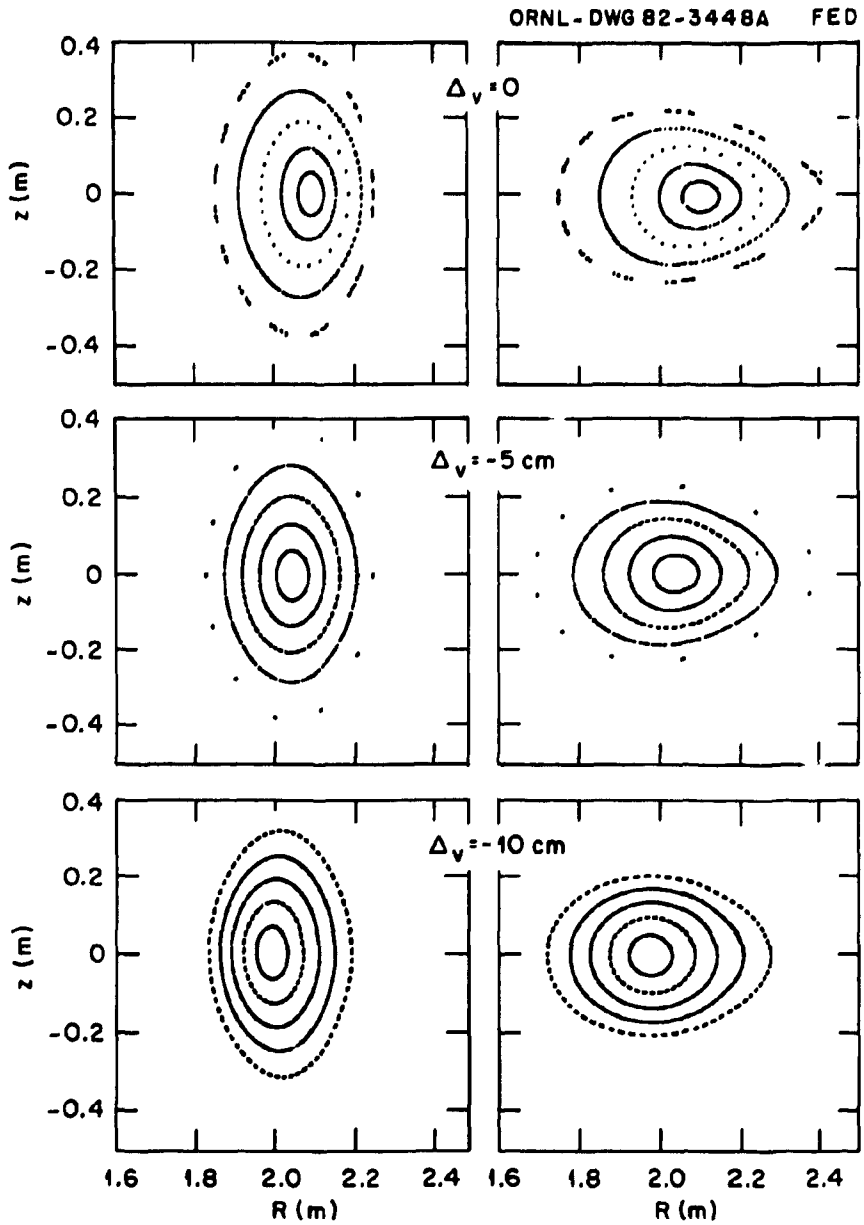
ORNL-DWG 82-3448A FED
Δ_v=0
Δ_v=-5 cm
Δ_v=-10 cm
z (m)
0.4
0.2
0
-0.2
-0.4
1.6
1.8
2.0
2.2
2.4
R (m)

Fig. 3

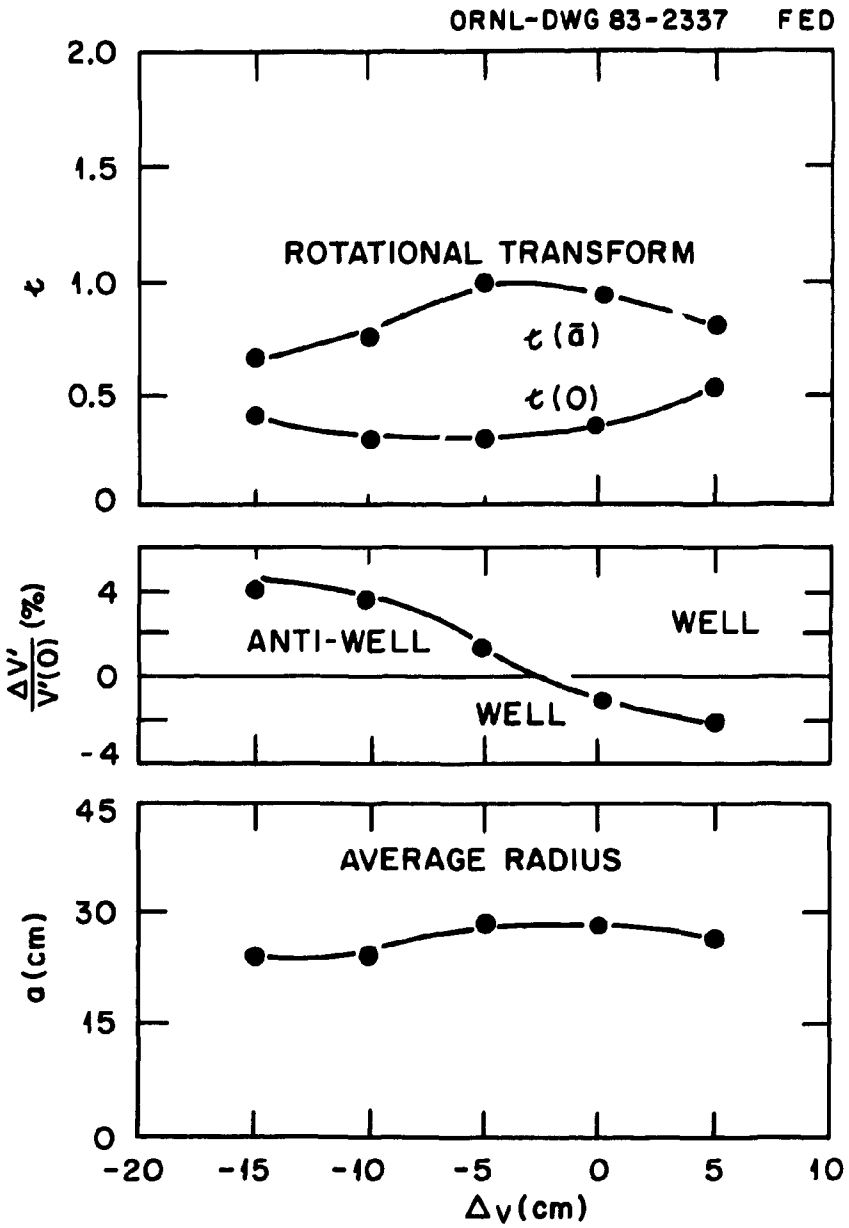
ORNL-DWG 83-2337 FED
ROTATIONAL TRANSFORM
t
t(ā)
t(0)
2.0
1.5
1.0
0.5
0
ANTI-WELL
WELL
WELL
4
0
-4
ΔV'/V'(0) (%)
AVERAGE RADIUS
a(cm)
45
30
15
0
-20
-15
-10
-5
0
5
10
Δv(cm)

Fig. 4

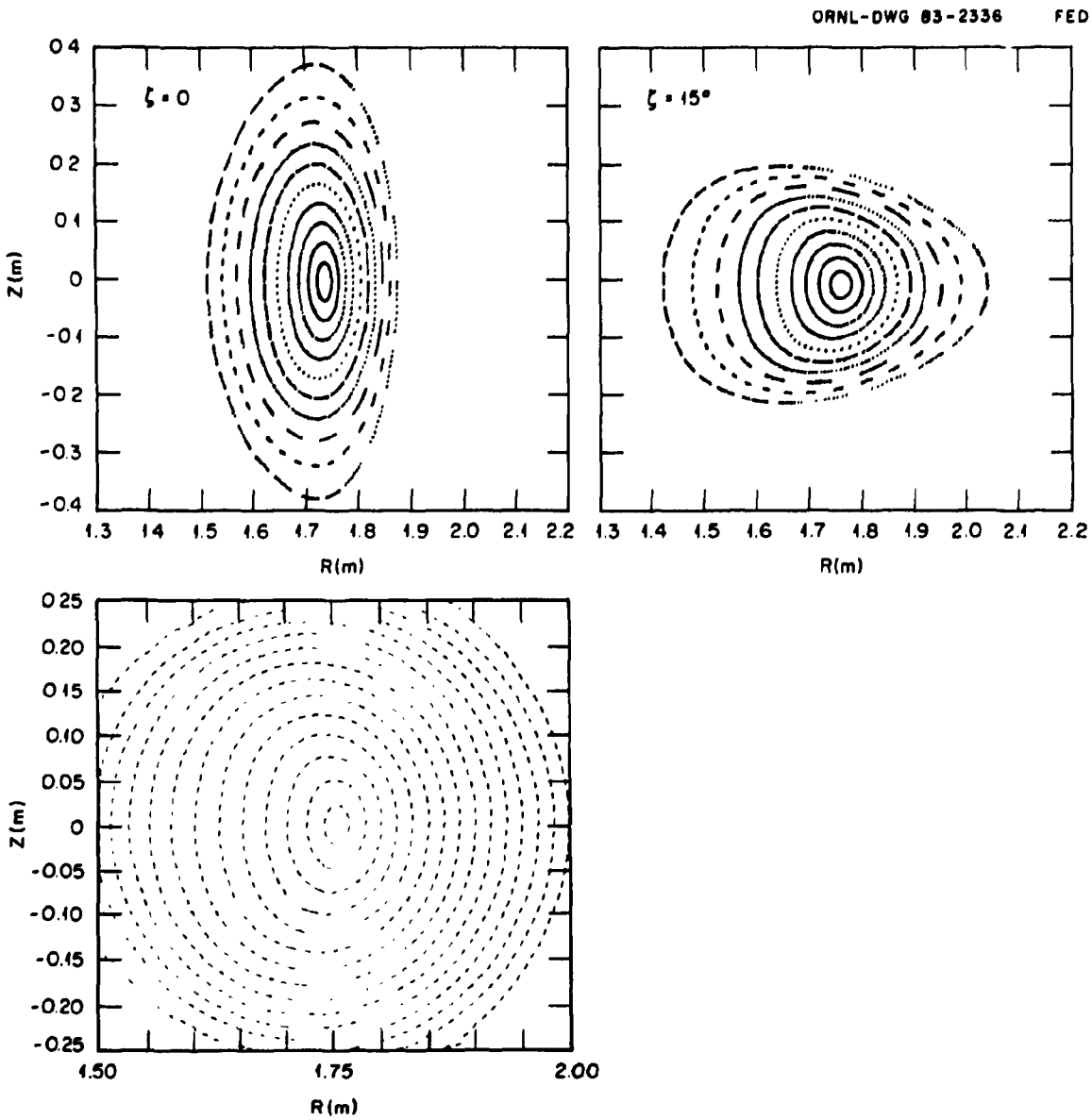
ORNL-DWG 83-2336 FED
ζ = 0
ζ = 15°
Z(m)
R(m)
0.4
0.3
0.2
0.1
0
-0.1
-0.2
-0.3
-0.4
1.3 1.4 1.5 1.6 1.7 1.8 1.9 2.0 2.1 2.2
0.25
0.20
0.15
0.10
0.05
-0.05
-0.10
-0.15
-0.20
-0.25
1.50 1.75 2.00

Fig. 5

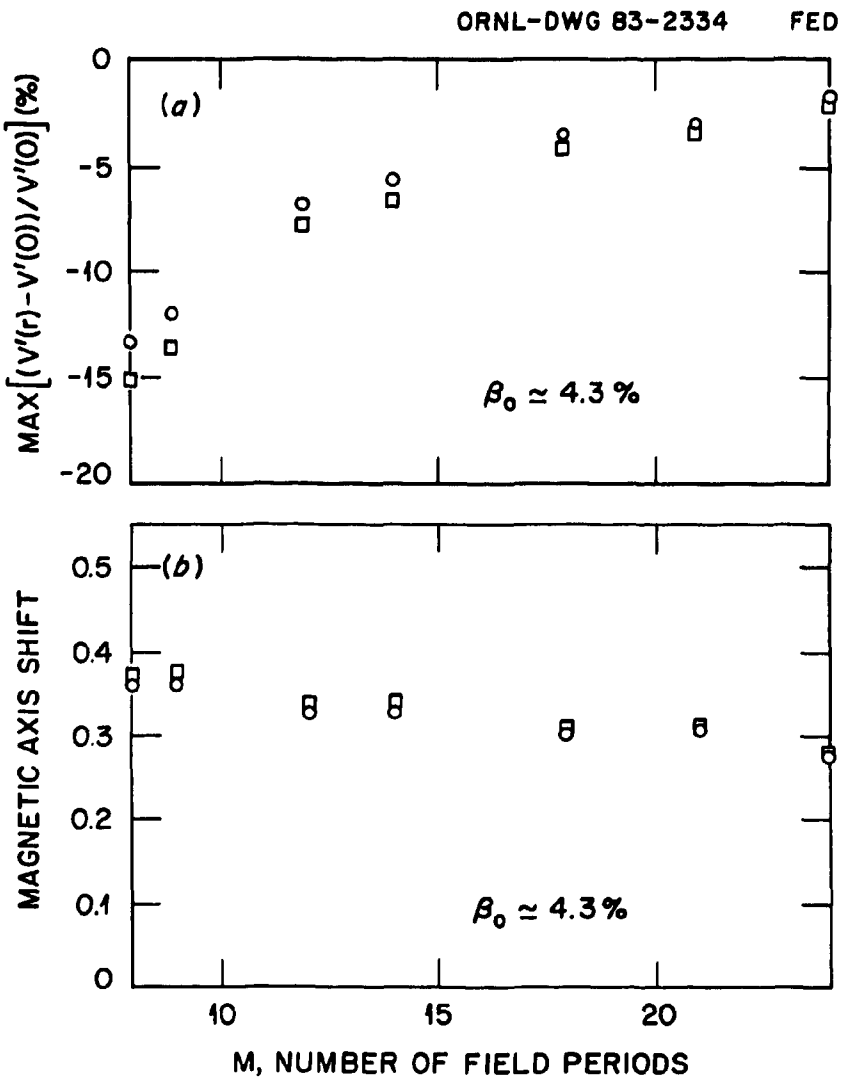
ORNL-DWG 83-2334 FED
(a)
MAX[(V'(r)-V'(0))/V'(0)](%)
0
-5
-10
-15
-20
$\beta_0 \simeq 4.3\,\%$
(b)
MAGNETIC AXIS SHIFT
0.5
0.4
0.3
0.2
0.1
0
$\beta_0 \simeq 4.3\,\%$
10
15
20
M, NUMBER OF FIELD PERIODS

Fig. 6

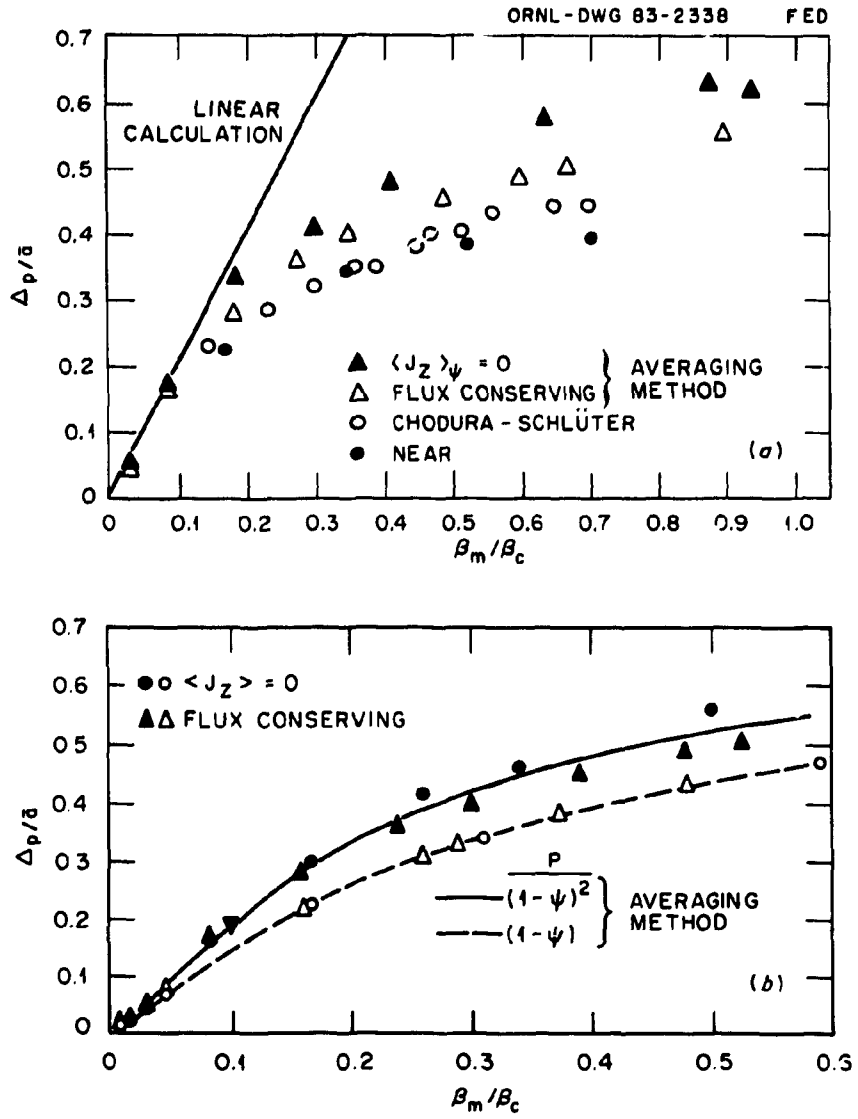
ORNL-DWG 83-2338 FED
LINEAR CALCULATION
$\langle J_z \rangle_\psi = 0$
FLUX CONSERVING
AVERAGING METHOD
CHODURA - SCHLÜTER
NEAR
(a)
Δ_p/a
β_m/β_c
$\langle J_z \rangle = 0$
FLUX CONSERVING
$\frac{P}{(1-\psi)^2}$
$(1-\psi)$
AVERAGING METHOD
(b)

Fig. 7

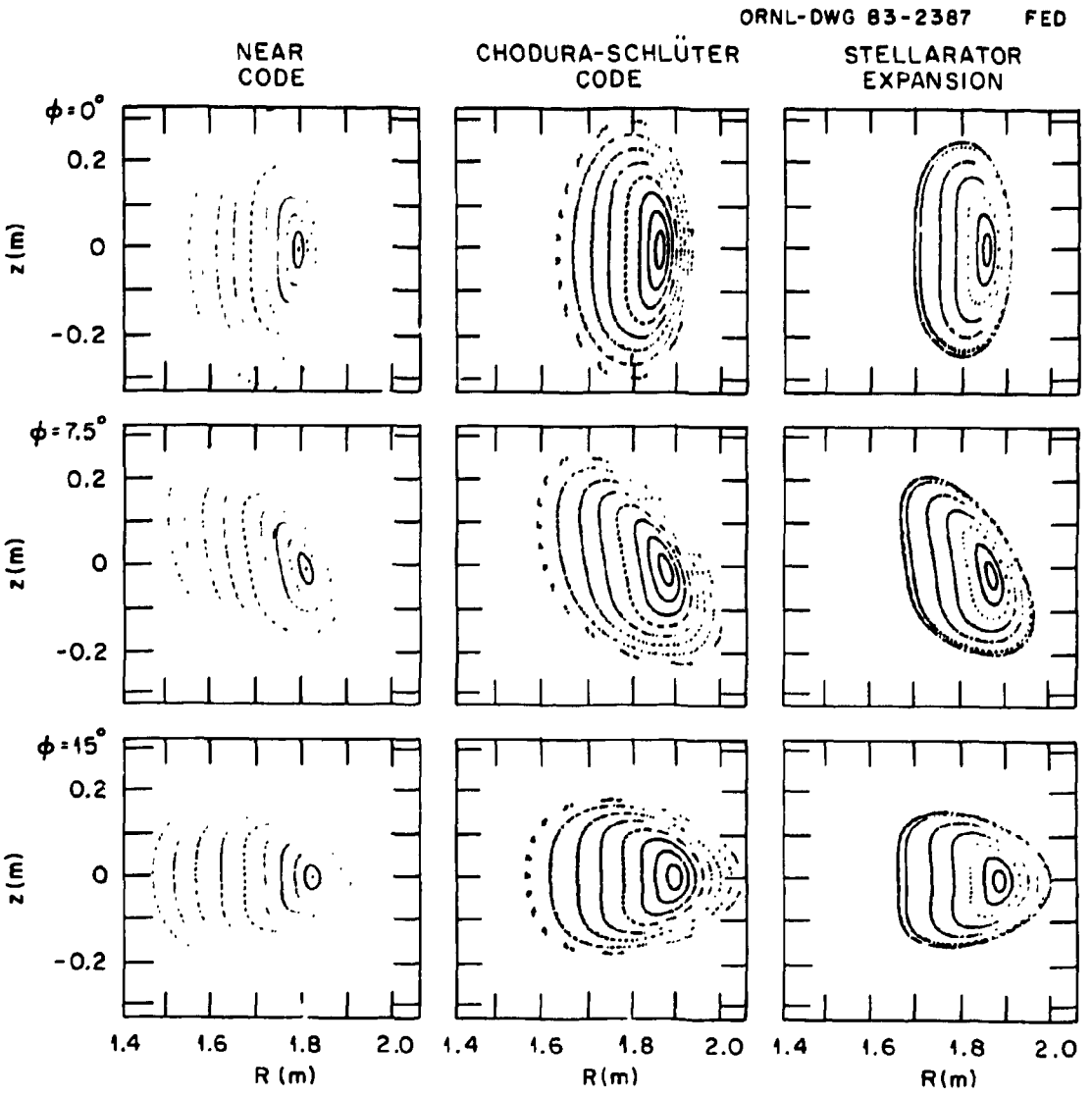
ORNL-DWG 83-2387 FED
NEAR CODE
CHODURA-SCHLÜTER CODE
STELLARATOR EXPANSION
φ=0°
φ=7.5°
φ=15°
z (m)
0.2
0
-0.2
1.4
1.6
1.8
2.0
R (m)
R(m)

Fig. 8

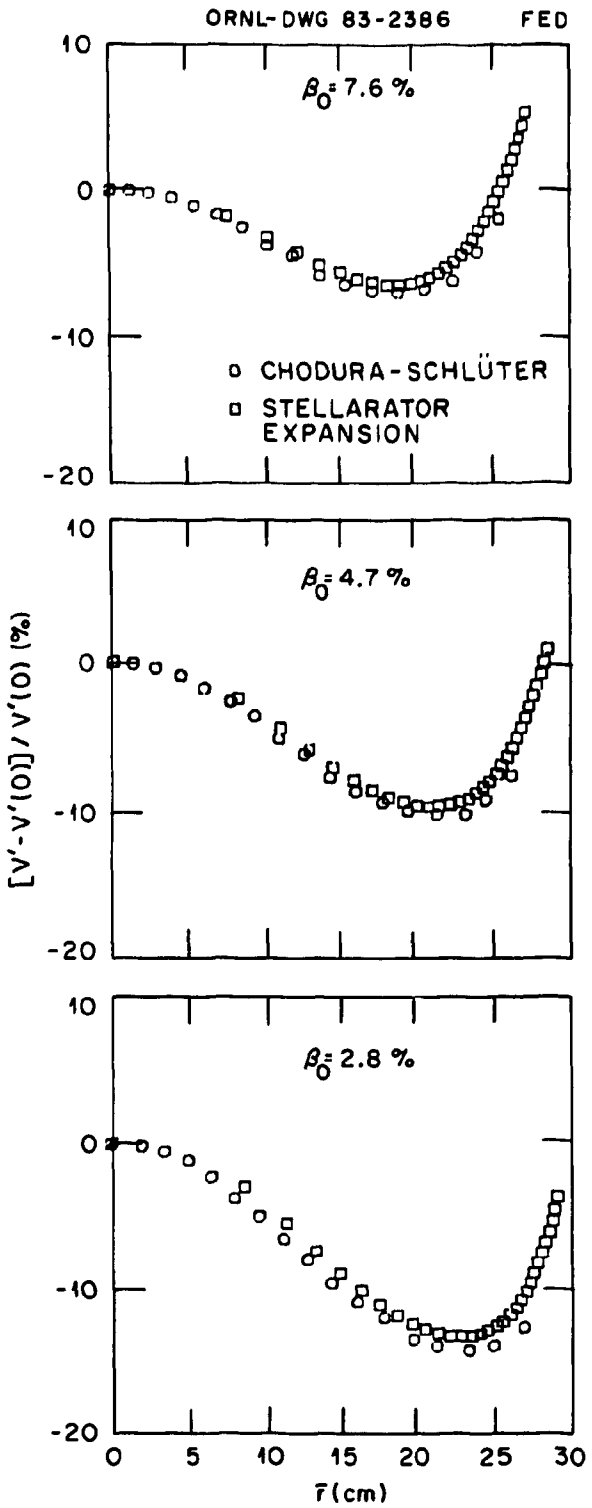
ORNL-DWG 83-2386 FED
β_0 = 7.6 %
β_0 = 4.7 %
β_0 = 2.8 %
CHODURA-SCHLÜTER
STELLARATOR EXPANSION
[V'-V'(0)] / V'(0) (%)
r̄(cm)
10
0
-10
-20
0
5
10
15
20
25
30

Fig. 9

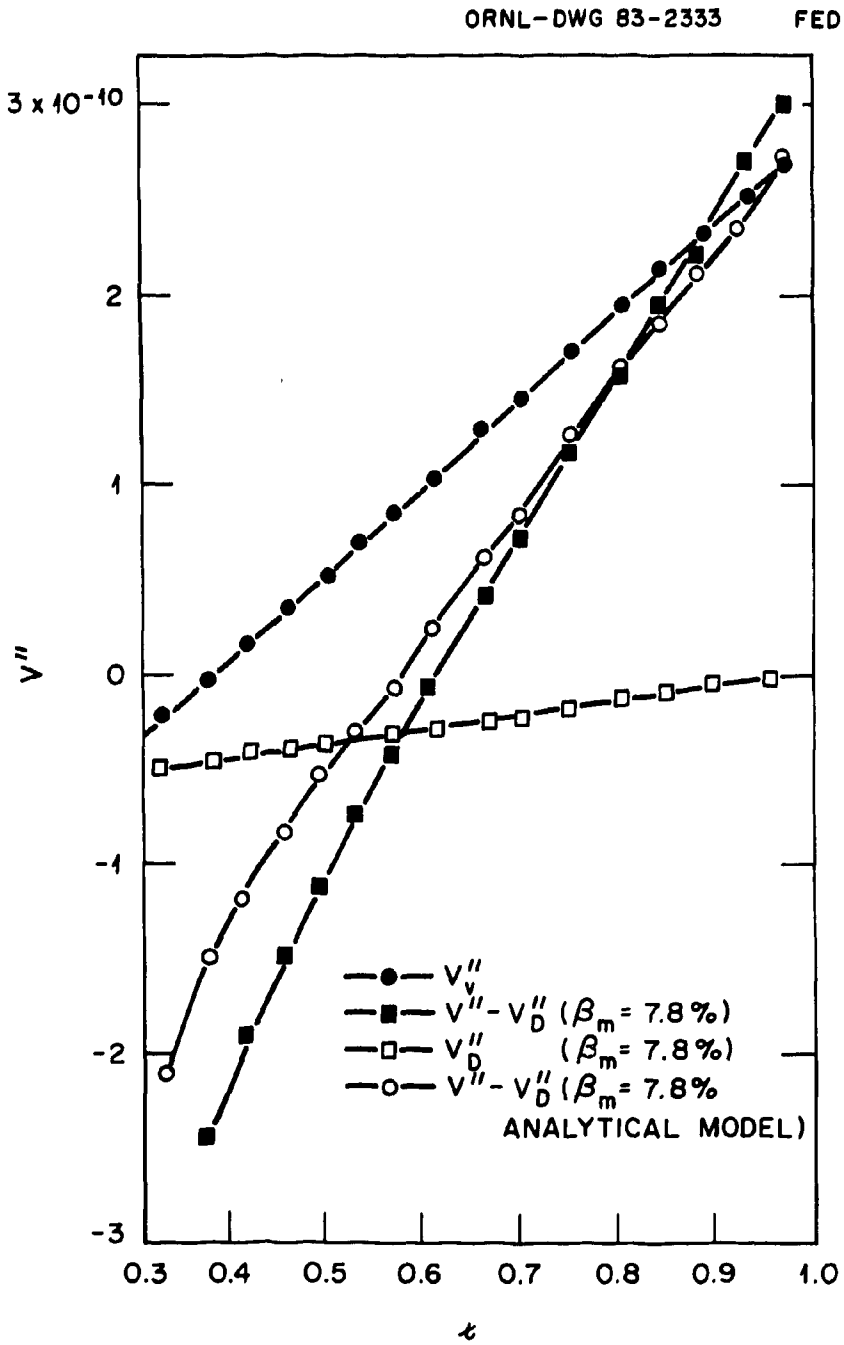
ORNL-DWG 83-2333 FED
3 x 10⁻¹⁰
2
1
0
-1
-2
-3
V''
0.3
0.4
0.5
0.6
0.7
0.8
0.9
1.0
x
V''v
V''- V''D (βm = 7.8 %)
V''D (βm = 7.8 %)
V''- V''D (βm = 7.8 % ANALYTICAL MODEL)

Fig. 10

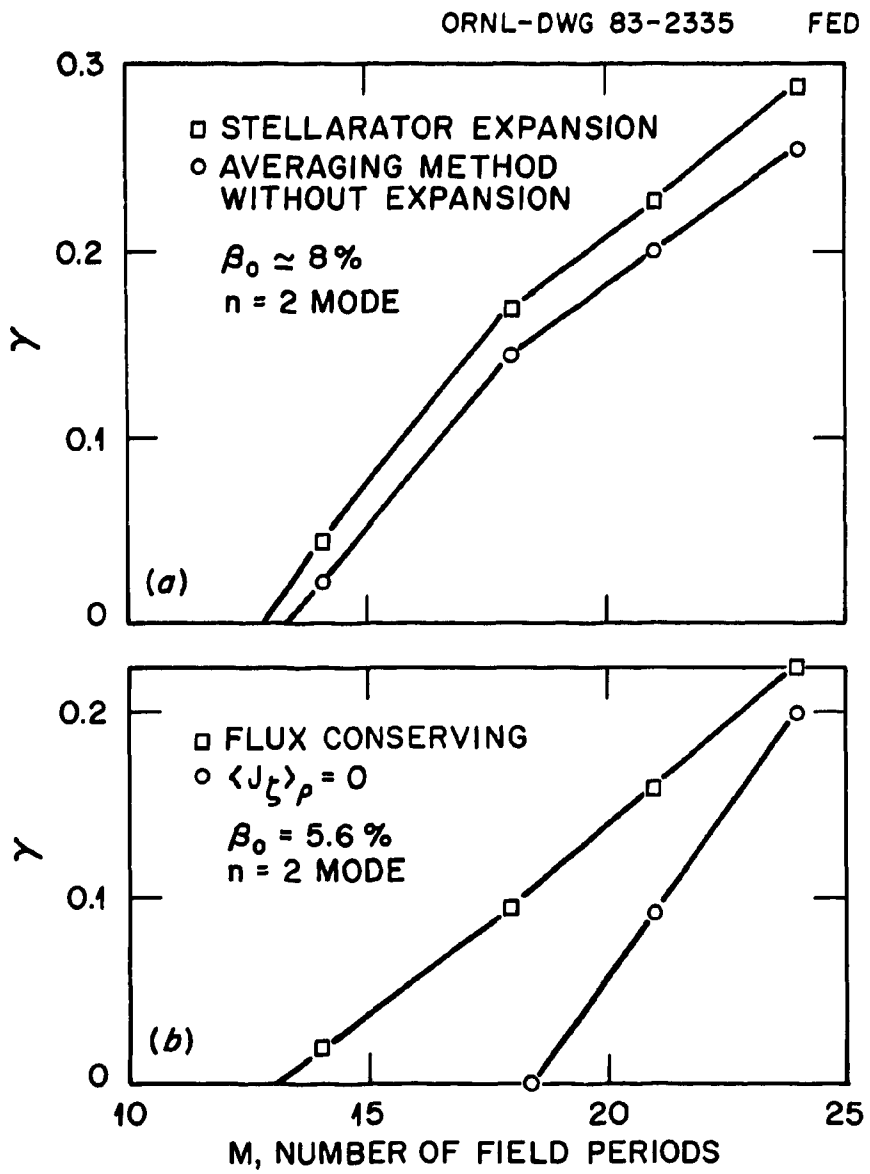
ORNL-DWG 83-2335 FED
0.3
0.2
0.1
0
γ
□ STELLARATOR EXPANSION
○ AVERAGING METHOD WITHOUT EXPANSION
$\beta_0 \simeq 8\%$
n = 2 MODE
(a)
0.2
0.1
0
γ
□ FLUX CONSERVING
○ $\langle J_\zeta \rangle_\rho = 0$
$\beta_0 = 5.6\%$
n = 2 MODE
(b)
10
15
20
25
M, NUMBER OF FIELD PERIODS

Fig. 11

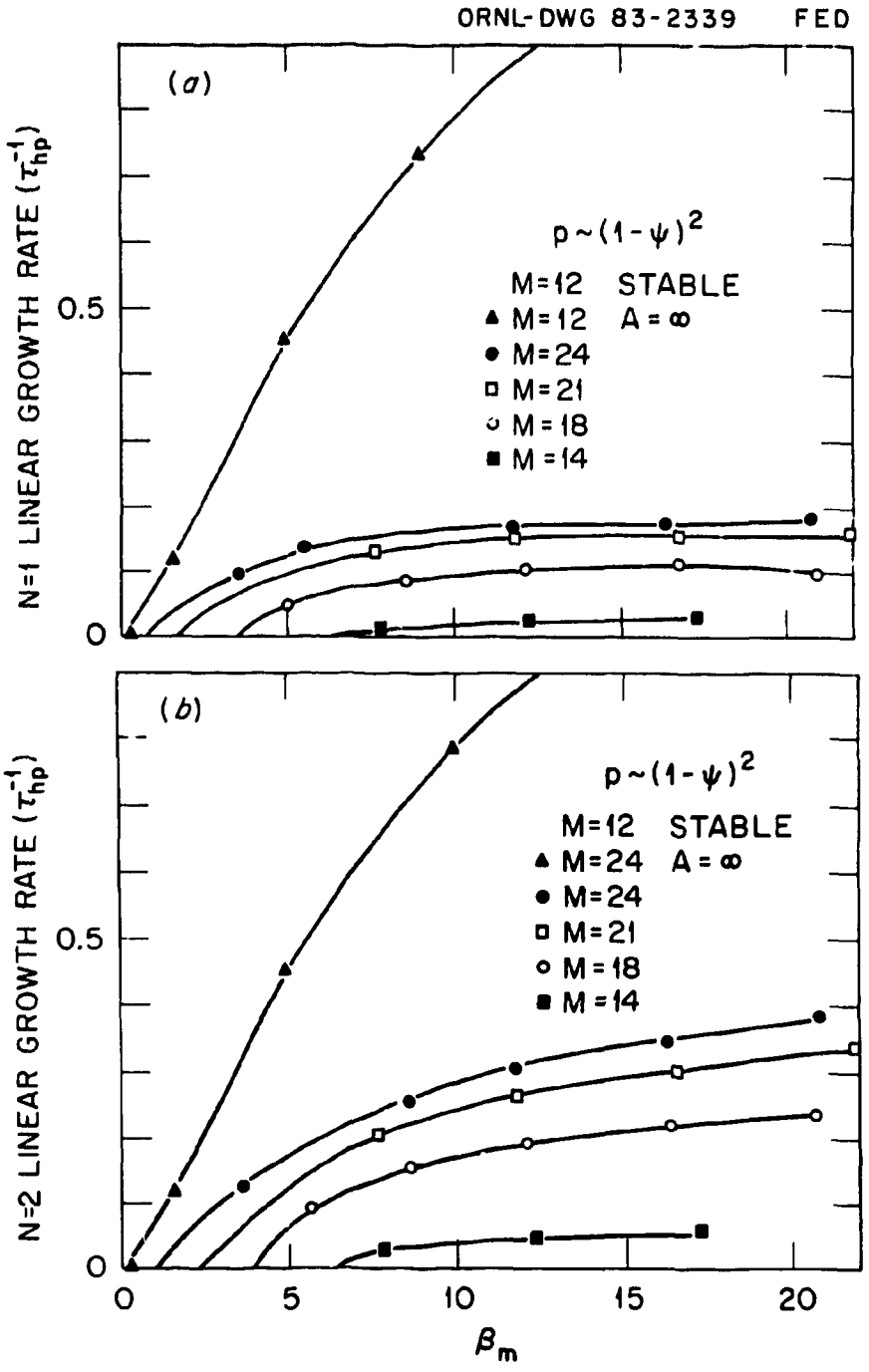
ORNL-DWG 83-2339 FED
(a)
N=1 LINEAR GROWTH RATE (τ_{hp}^{-1})
$p \sim (1-\psi)^2$
M=12 STABLE
M=12 A = ∞
M=24
M=21
M=18
M=14
0.5
0
(b)
N=2 LINEAR GROWTH RATE (τ_{hp}^{-1})
$p \sim (1-\psi)^2$
M=12 STABLE
M=24 A = ∞
M=24
M=21
M=18
M=14
0.5
0
0
5
10
15
20
β_m

Fig. 12

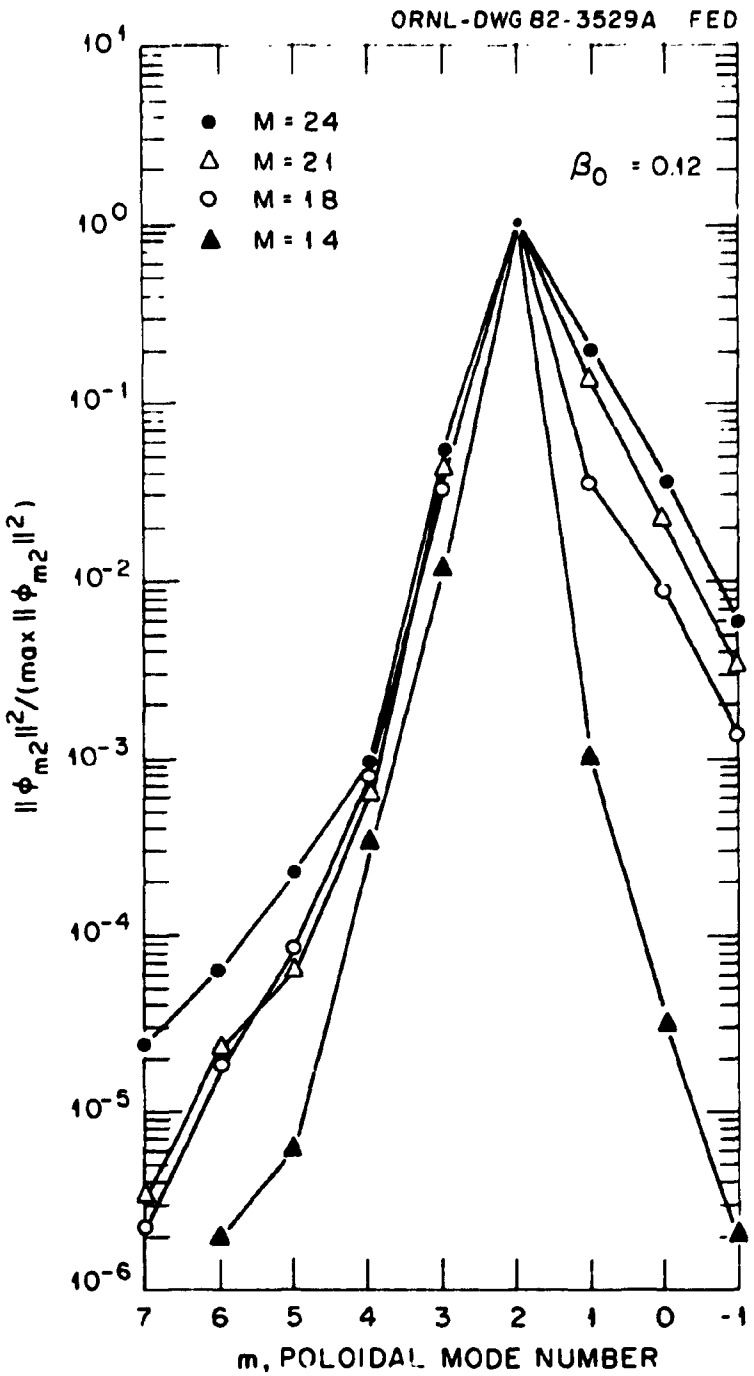
ORNL-DWG 82-3529A FED
M = 24
M = 21
M = 18
M = 14
β_0 = 0.12
10^1
10^0
10^{-1}
10^{-2}
10^{-3}
10^{-4}
10^{-5}
10^{-6}
$\|\phi_{m2}\|^2/(\max \|\phi_{m2}\|^2)$
7 6 5 4 3 2 1 0 -1
m, POLOIDAL MODE NUMBER

Fig. 13

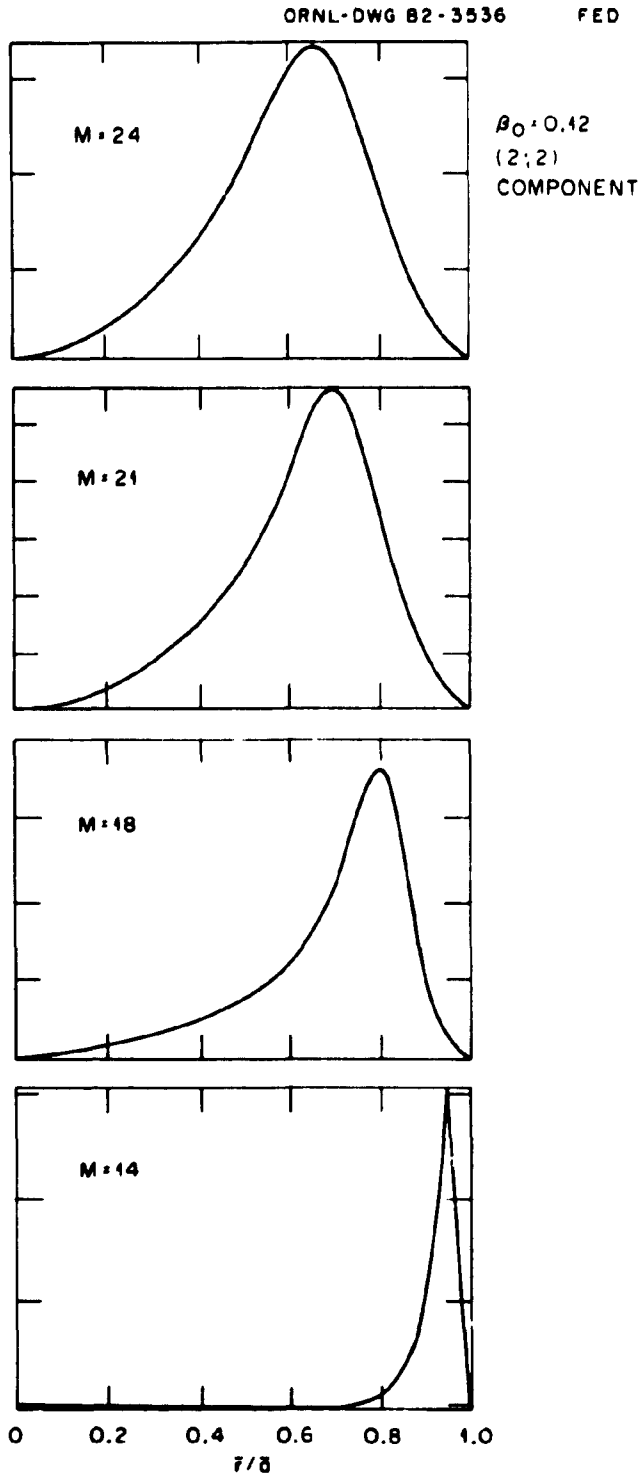
ORNL-DWG 82-3536 FED
M = 24
M = 21
M = 18
M = 14
$\beta_0 = 0.12$
(2;2)
COMPONENT
0
0.2
0.4
0.6
0.8
1.0
r/a

Fig. 14

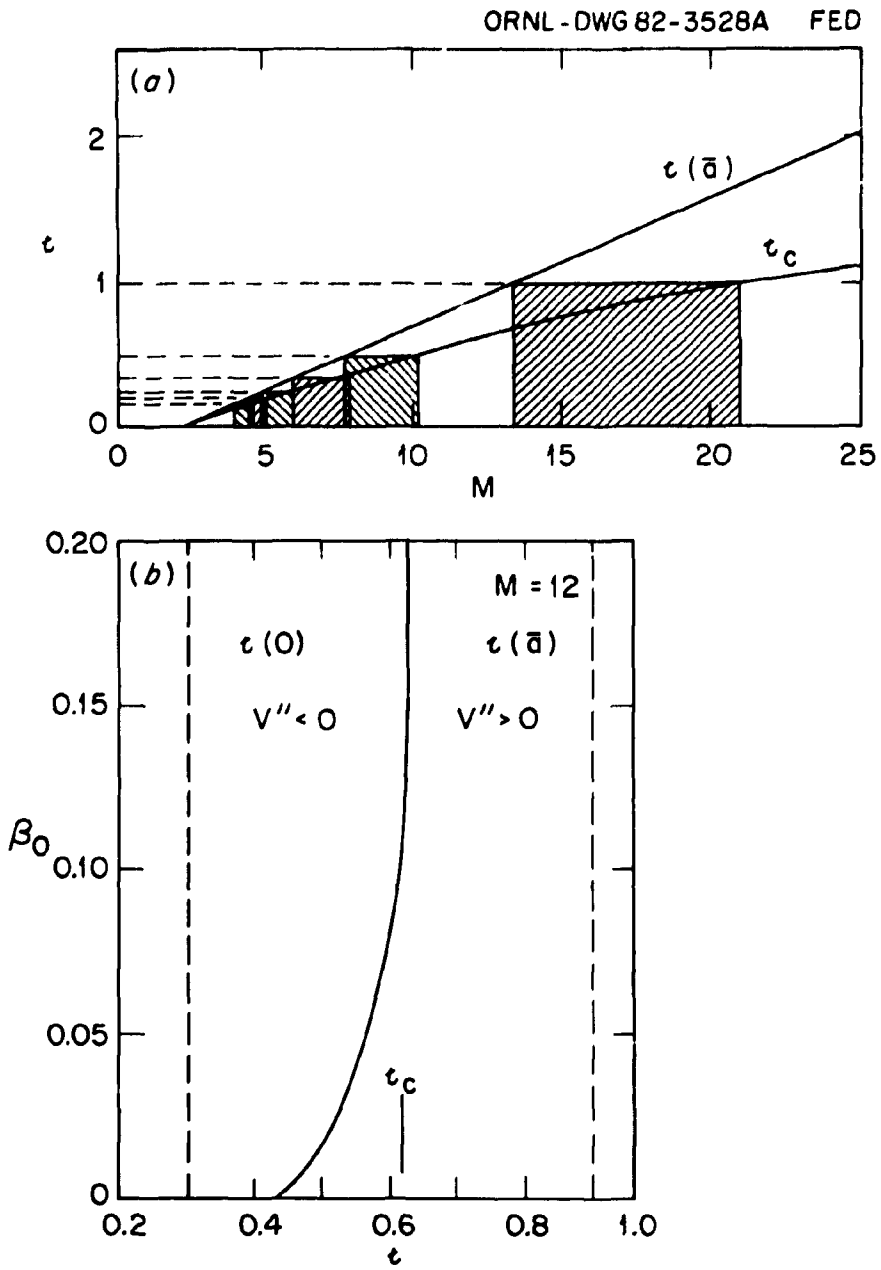
ORNL-DWG 82-3528A FED
(a)
t
2
1
0
t (ā)
t_c
0
5
10
15
20
25
M
(b)
M = 12
t (0)
t (ā)
V″ < 0
V″ > 0
β_0
0.20
0.15
0.10
0.05
0
t_c
0.2
0.4
0.6
0.8
1.0
t

Fig. 15

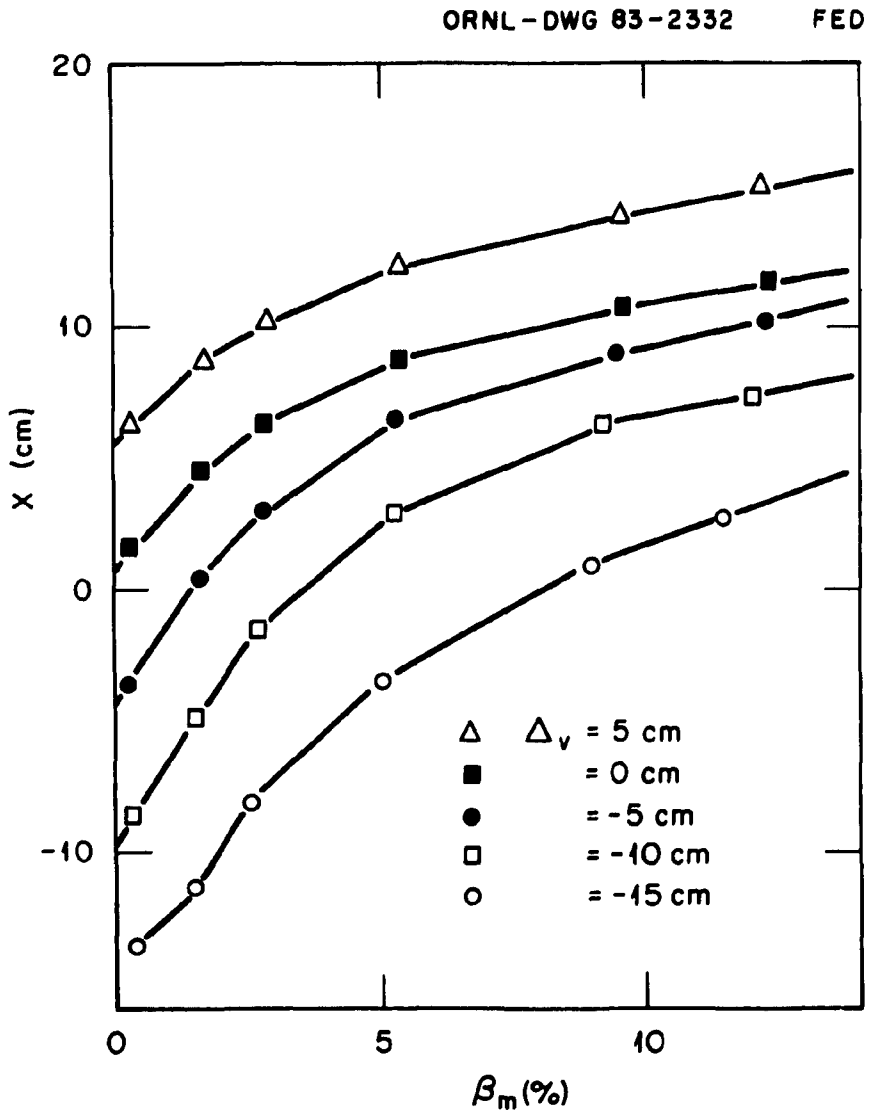
ORNL-DWG 83-2332 FED
20
10
0
-10
x (cm)
0
5
10
β_m(%)
Δ_v = 5 cm
= 0 cm
= -5 cm
= -10 cm
= -15 cm

Fig. 16

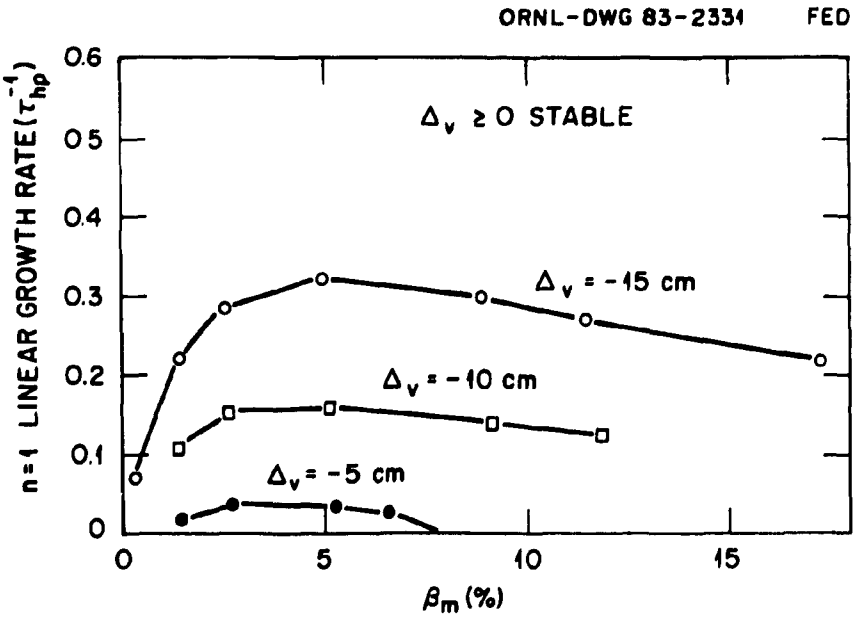
ORNL-DWG 83-2331 FED
n=1 LINEAR GROWTH RATE(τ_{hp}^{-1})
0.6
0.5
0.4
0.3
0.2
0.1
0
$\Delta_v \geq 0$ STABLE
$\Delta_v = -15$ cm
$\Delta_v = -10$ cm
$\Delta_v = -5$ cm
0
5
10
15
β_m (%)

Fig. 17

ORNL/TM-8752
Dist. Category UC-20 g

INTERNAL DISTRIBUTION

1-5. B. A. Carreras
6. R. A. Dory
7. J. Dunlap
8. L. Garcia
9. J. H. Harris
10. T. C. Hender
11. H. R. Hicks
12. J. A. Holmes
13. V. E. Lynch
14. B. F. Masden
15. Y-K. M. Peng
16. J. Sheffield
17. D. Sigmar
18-19. Laboratory Records Department
20. Laboratory Records, ORNL-RC
21. Document Reference Section
22. Central Research Library
23. Fusion Energy Division Library
24. Fusion Energy Division Reports Office
25. ORNL Patent Office

EXTERNAL DISTRIBUTION

26. Office of the Assistant Manager for Energy Research and Development, Department of Energy, Oak Ridge Operations, Box E, Oak Ridge, TN 37830
27. J. D. Callen, Department of Nuclear Engineering, University of Wisconsin, Madison, WI 53706
28. R. W. Conn, Department of Chemical, Nuclear, and Thermal Engineering, University of California, Los Angeles, CA 90024
29. S. O. Dean, Director, Fusion Energy Development, Science Applications, Inc., 2 Professional Drive, Gaithersburg, MD 20760
30. H. K. Forsen, Bechtel Group, Inc., Research Engineering, P.O. Box 3965, San Francisco, CA 94105
31. R. W. Gould, Department of Applied Physics, California Institute of Technology, Pasadena, CA 91125
32. D. G. McAlees, Exxon Nuclear Company, Inc., 777 106th Avenue, NE, Bellevue, WA 98009
33. P. J. Reardon, Princeton Plasma Physics Laboratory, P.O. Box 451, Princeton, NJ 08540
34. W. M. Stacey, Jr., School of Nuclear Engineering, Georgia Institute of Technology, Atlanta, GA 30332
35. G. A. Eliseev, I. V. Kurchatov Institute of Atomic Energy, P.O. Box 3402, 123182 Moscow, U.S.S.R.
36. V. A. Glukhikh, Scientific-Research Institute of Electro-Physical Apparatus, 188631 Leningrad, U.S.S.R.
37. I. Spighel, Lebedev Physical Institute, Leninsky Prospect 53, 117924 Moscow, U.S.S.R.
38. D. D. Ryutov, Institute of Nuclear Physics, Siberian Branch of the Academy of Sciences of the U.S.S.R., Sovetskaya St. 5, 630090 Novosibirsk, U.S.S.R.
39. V. T. Tolok, Kharkov Physical-Technical Institute, Academical St. 1, 310108 Kharkov, U.S.S.R.

40. R. Varma, Physical Research Laboratory, Navangpura, Ahmedabad, India
41. Bibliothek, Max-Planck Institut fur Plasmaphysik, D-8046 Garching bei Munchen, Federal Republic of Germany
42. Bibliothek, Institut fur Plasmaphysik, KFA, Postfach 1913, D-5170 Julich, Federal Republic of Germany
43. Bibliotheque, Centre de Recherches en Physique des Plasmas, 21 Avenue des Bains, 1007 Lausanne, Switzerland
44. Bibliotheque, Service du Confinement des Plasmas, CEA, B.P. 6, 92 Fontenay-aux-Roses (Seine), France
45. Documentation S.I.G.N., Departement de la Physique du Plasma et de la Fusion Controlee, Centre d'Etudes Nucleaires, B.P. No. 85, Centre du Tri, 38041 Cedex, Grenoble, France
46. Library, Culham Laboratory, UKAEA, Abingdon, Oxon, OX14 3DB, England
47. Library, FOM Institut voor Plasma-Fysica, Rijnhuizen, Jutphaas, The Netherlands
48. Library, Institute of Physics, Academia Sinica, Beijing, Peoples Republic of China
49. Library, Institute of Plasma Physics, Nagoya University, Nagoya 64, Japan
50. Library, International Centre for Theoretical Physics, Trieste, Italy
51. Library, Laboratorio Gas Ionizzati, Frascati, Italy
52. Library, Plasma Physics Laboratory, Kyoto University, Gokasho Uji, Kyoto, Japan
53. Plasma Research Laboratory, Australian National University, P.O. Box 4, Canberra, A.C.T. 2000, Australia
54. Thermonuclear Library, Japan Atomic Energy Research Institute, Tokai, Naka, Ibaraki, Japan
55. J. F. Clarke, Associate Director for Fusion Energy, Office of Fusion Energy, Office of Energy Research, Mail Stop G-256, U.S. Department of Energy, Washington, DC 20545
56. J. F. Decker, Director, Division of Applied Plasma Physics, Office of Fusion Energy, Office of Energy Research, Mail Stop G-256, U.S. Department of Energy, Washington, DC 20545
57. D. B. Nelson, Fusion Theory and Computer Services Branch, Office of Fusion Energy, Office of Energy Research, Mail Stop G-256, U.S. Department of Energy, Washington, DC 20545
58. M. N. Rosenbluth, RLM 11.218, Institute for Fusion Studies, University of Texas, Austin, TX 78712
59. W. Sadowski, Fusion Theory and Computer Services Branch, Office of Fusion Energy, Office of Energy Research, Mail Stop G-256, U.S. Department of Energy, Washington, DC 20545
60. N. A. Davies, Tokamak Systems Branch, Office of Fusion Energy, Office of Energy Research, Mail Stop G-256, U.S. Department of Energy, Washington, DC 20545
61. E. Oktay, Tokamak Systems Branch, Office of Fusion Energy, Office of Energy Research, Mail Stop G-256, U.S. Department of Energy, Washington, DC 20545
62. Theory Department Read File, c/o D. W. Ross, Institute for Fusion Studies, University of Texas at Austin, Austin, TX 78712

63. Theory Department Read File, c/o R. C. Davison, Director, Plasma Fusion Center, 167 Albany Street, Cambridge, MA 02139
64. Theory Department Read File, c/o F. W. Perkins, Princeton Plasma Physics Laboratory, P.O. Box 451, Princeton, NJ 08540
65. Theory Department Read File, c/o L. Kovrizhnykh, Lebedev Institute of Physics, Academy of Sciences, 53 Leninsky Prospect, Moscow, U.S.S.R. V312
66. Theory Department Read File, c/o B. B. Kadomtsev, I. V. Kurchatov Institute of Atomic Energy, P.O. Box 3402, Moscow, U.S.S.R. 123182
67. Theory Department Read File, c/o T. Kamimura, Institute of Plasma Physics, Nagoya University, Nagoya, Japan
68. Theory Department Read File, c/o C. Mercier, Euratom-CEA, Service de Recherches sur la Fusion Controlee, Fontenay-aux-Roses (Seine), France
69. Theory Department Read File, c/o T. E. Stringer, JET Joint Undertaking, Culham Laboratory, Abingdon, Oxon, OX14 3DB, England
70. Theory Department Read File, c/o K. Roberts, Culham Laboratory, Abingdon, Oxon, OX14 3DB, England
71. Theory Department Read File, c/o D. Biskamp, Max-Planck-Institut fur Plasmaphysik, D-8046 Garching bei Munchen, Federal Republic of Germany
72. Theory Department Read File, c/o T. Takeda, Japan Atomic Energy Research Institute, Tokai, Naka, Ibaraki, Japan
73. Theory Department Read File, c/o C. S. Liu, General Atomic Company, P.O. Box 81608, San Diego, CA 92138
74. Theory Department Read File, c/o L. D. Pearlstein, Lawrence Livermore National Laboratory, P.O. Box 808, Livermore, CA 94550
75. Theory Department Read File, c/o R. Gerwin, CTR Division, MS 640, Los Alamos National Laboratory, P.O. Box 1663, Los Alamos, NM 87545

76-247. Given distribution as shown in TID-4500 Magnetic Fusion Energy (Category Distribution UC-20 g: Theoretical Plasma Physics)